

The Quantum Gas Microscope

A dissertation presented

by

Jonathon Isaiah Gillen

to

The Department of Physics

in partial fulfillment of the requirements

for the degree of

Doctor of Philosophy

in the subject of

Physics

Harvard University

Cambridge, Massachusetts

October 2009

©2009 - Jonathon Isaiah Gillen

All rights reserved.

Thesis advisor

Author

Markus Greiner

Jonathon Isaiah Gillen

The Quantum Gas Microscope

Abstract

We demonstrate single site detection of ultra cold atoms in a two dimensional optical lattice. A high numerical aperture imaging system allows us to probe the atoms in a two dimensional optical lattice with an unprecedented resolution of $\sim 500\text{nm}$. In contrast to previous experiments with large lattice spacings of $5\mu\text{m}$ or larger we demonstrate single site addressability in an optical lattice with significant tunnel coupling, making this system suitable for the study of many body physics. Exploiting our high numerical aperture system we also demonstrate a new method of lattice projection. Using our imaging system in reverse, we holographically project two dimensional lattice potentials onto the atoms. This method is very flexible and not limited to the projection of lattices. In fact arbitrary potentials may be projected onto the atoms allowing for the creation of complex many body states. On our march towards single site detection we demonstrate the most successful evanescent wave surface trap to date, achieving strong confinement with long lifetimes and negligible heating rates. We also demonstrate the use of broadband light for the trapping and manipulation of ultra cold atoms to avoid the ill effects of stray light in our optical potentials.

Contents

Title Page	i
Abstract	iii
Table of Contents	iv
Acknowledgments	vii
Dedication	viii
1 Introduction and summary	1
1.1 Introduction	1
1.2 Single site resolution	3
1.3 Concept	4
1.4 Organization of this thesis	8
2 Theory	10
2.1 Bose-Einstein condensates	10
2.1.1 Intro	10
2.1.2 Dimensionality	10
2.1.3 Interacting BEC	11
2.1.4 Thomas-Fermi approximation	12
2.1.5 Dimensionality revisited	13
2.1.6 2D Bose condensation	15
2.2 Optical lattices	15
2.2.1 Optical potentials	15
2.2.2 Gaussian beams	17
2.2.3 Periodic optical potentials	17
2.3 Band structure	18
2.3.1 Bloch's theorem	20
2.3.2 Wannier functions	20
2.4 Bose-Hubbard Hamiltonian	22
2.5 Mott insulator	23

3	Creation of a Bose-Einstein condensate	24
3.1	Overview	24
3.2	Laser setup	25
3.3	Vacuum chamber	25
3.4	Assembly and bakeout procedure	27
3.5	Magneto-optical trap	28
3.6	Magnetic transport	30
3.7	RF evaporation	30
3.8	BEC production sequence	30
4	Magnetic field control	33
4.1	Introduction	33
4.2	Magnetic trapping of neutral atoms	33
4.3	Quadrupole traps	34
4.4	Magnetic transport	35
4.4.1	Calculation of currents	36
4.4.2	Circuitry for magnetic field control	37
4.4.3	Physical design of coils	37
4.5	QUIC trap	37
4.5.1	QUIC topology	38
4.5.2	Physical design of QUIC trap	41
4.6	Controlling the trap position in the spherical trap	42
5	Evanescent wave surface trap	46
5.1	Introduction	46
5.2	Evanescent waves	47
5.3	Susceptibility of evanescent waves to surface scatter and uncontrolled interferences	49
5.3.1	Broadband light	49
5.3.2	Superpolished substrate	51
5.3.3	Adsorbates on superpolished surface	51
5.3.4	General lab cleanliness	52
5.3.5	Mechanical mounting of the hemisphere	52
5.4	Loading the evanescent wave surface trap	54
5.5	Analysis and results	55
5.6	Summary and outlook	58
6	1D axial lattice	59
6.1	Introduction	59
6.2	Comparison of evanescent wave trap to standing wave trap	60
6.3	Axial lattice surface trap	61
6.4	Setup	61

6.5	Characterization of quantum gas in the 2D regime	63
6.6	RF evaporation in the standing wave	64
6.7	RF spectroscopy in the 1D lattice	65
6.8	Summary	66
7	2D Lattice and imaging	68
7.1	Introduction	68
7.2	Imaging system	69
7.3	Mounting of the microscope objective	70
7.4	Holographic projection of lattices	72
	7.4.1 2D lattice setup	73
7.5	Optical molasses	74
7.6	Detection sequence	76
7.7	Results	78
7.8	Conclusions	81
7.9	Outlook	82
	Bibliography	83
	A Rubidium data	90
	B Anti-reflection coating curves	95

Acknowledgments

Coming to Harvard for graduate school was one of the best decisions of my life. Much to my delight, I arrived to find a department full of energy and excitement with the support structure necessary to get things done. I am acutely aware of the fact that my thesis work would not have been possible without all of the wonderful help I received along the way and I will do my best to give thanks to everyone involved. I would like to begin by thanking my thesis advisor Markus Greiner for offering me such an exciting and stimulating research topic for my thesis as well as being a wonderful advisor and friend. I would also like to thank my labmates over the years for all of their contributions to this work - Waseem Bakr, Peter Unterwaditzer, Hannes Brachmann, Amy Peng, Simon Fölling, and Ed Su. Outside of the lab I would like to give a special thanks to Stan Cotreau, Victoria Greene, William Walker, and Stuart McNeil who helped make the department feel like a second home for me. Sheila Ferguson also deserves a very special thanks for looking after me for all these years and for being there when I needed her the most. Thanks to Rebecca, William, Dan, and Lee for their unwavering support and last but not least I would like to thank my wife Yi-Chia for all of her support and love.

Dedicated to my mother.

Chapter 1

Introduction and summary

”The existence of a periodic lattice of ions lies at the heart of modern solid state physics. It provides the basis for the entire analytic framework of the subject, and without it comparatively little progress would have been made. If there is any one reason why the theory of solids is so much more highly developed than the theory of liquids, even though both forms of matter have comparable densities, it is that the ions are arranged periodically in the solid state but are spatially disordered in liquids. It is the lack of a periodic array of ions that has left the subject of amorphous solids in so primitive a state compared with the highly developed theory of crystalline solids.” [5]

1.1 Introduction

Ultracold atoms in optical lattices present an exciting new platform to study condensed matter physics. Following the proposal of Jaksch *et al.* [45], the realization of the Bose-Hubbard Hamiltonian with ultra cold atoms in optical lattices was im-

plemented shortly after [35]. What followed has been an exciting period in atomic physics with a common goal of implementing condensed matter Hamiltonians as a guiding light [15].

To realize a model system for condensed matter, we begin by replacing the electrons bound to the periodically spaced ions in a real crystal with ultra cold atoms bound by an optical lattice potential. Model systems created in this way are very clean with none of the impurities found in real crystals. The interactions are well understood and can be calculated from first principles, allowing the implementation of simple Hamiltonians that can be readily compared with theory. Additionally, lattice parameters and interactions can be tuned dynamically [20, 81, 82, 33], offering a degree of flexibility not found in real crystals.

Cold thermal atoms in optical lattices have been studied for quite some time [46], but initial experiments were limited in two ways. Working with thermal clouds at temperatures in the μK regime meant not only that the atoms did not occupy the ground state of the lattice, but also that the filling factor of the lattice was quite low. Most efforts were focused on either cooling the sample down to the ground state after it was loaded into an optical lattice potential or increasing the low filling fraction that characterized these early experiments [23, 83]. With the experimental realization of Bose-Einstein condensate [3], an ultracold and dense sample of atoms became available for optical lattice experiments - offering a way to not only load the atoms into the ground state of the periodic potential, but also to realize high filling factors that had eluded previous experiments.

The first experiments to combine BEC with optical lattices began shortly after the

discovery of BEC in 1995. Initial experiments were performed using a one dimensional optical lattice combined with a BEC [2]. While these experiments did not suffer from low filling factors or high temperatures of earlier works, they did not have a large enough interaction energy per particle to observe many body physics. It was not until the experiments of Greiner *et al.* [35] that a BEC was loaded into an optical lattice with interactions comparable to or larger than the kinetic energy, leading to the first observation of a quantum phase transition from a superfluid to a Mott insulator. In years since the observation of the Mott insulator-superfluid phase transition, the number of groups studying optical lattices has skyrocketed - leading to many new and exciting results [11].

1.2 Single site resolution

Great progress has been made in the study of ultracold atoms in optical lattices in the past decade, with the number of tools to probe the system growing in complexity and number [11]. However, one feature currently lacking in optical lattice experiments aimed at studying many body physics is single site addressability. With single site addressability, we would be able to address and detect single atoms on individual lattice sites. In typical experiments where the atoms are released from the lattice and imaged after a short time of flight [60] this is not a possibility. A number of groups are currently working towards high resolution imaging systems to detect atoms on individual lattice sites *in situ*, but so far only one has succeeded [30] albeit with limited detection fidelity.

In our setup, single site addressability allows for the detection of single atoms

on individual lattice sites via *in situ* fluorescent imaging. It should be noted that any optical system capable of single site detection can in principle be used in reverse to project potentials at the single site level, allowing for the creation of novel lattice geometries, arbitrary potential landscapes, and local manipulations of internal degrees of freedom. Our very large numerical aperture of $\text{NA}=0.8$ allows us to take advantage of the aforementioned possibility and indeed we create our optical lattice potentials by using our imaging system in reverse.

Single site addressability has been achieved in systems with a large lattice spacing of $5\mu\text{m}$ or greater [62, 76] but these systems were not suitable for the study of many body physics due to their lack of tunnel coupling. This thesis reports the first results of the quantum gas microscope, capable of resolving individual lattice sites in a two dimensional optical lattice. Unlike previous experiments, we work in a regime where the lattice constant is small enough that we have a significant tunnel coupling, allowing us access to many-body physics.

1.3 Concept

The quantum gas microscope is a specialized BEC machine optimized for a very large optical access to the atoms. A multi-functional hemispheric optic is the centerpiece of the experimental design that facilitates both the creation of evanescent wave potentials which are instrumental in our creation of a 2D quantum gas as well as a solid immersion effect [57] that enhances the numerical aperture of the system by a factor of the index of refraction of the hemisphere.

In most BEC apparatuses the atoms sit deep inside of the vacuum chamber far

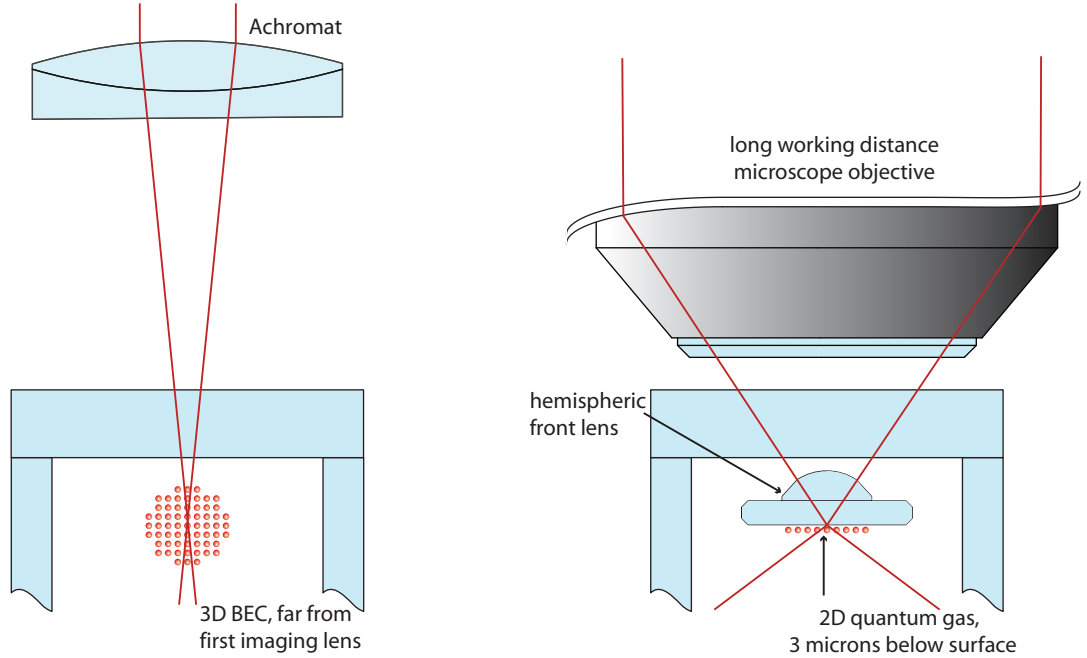


Figure 1.1: Schematic of quantum gas microscope concept. We create a 2D quantum gas a few microns away from a fused silica substrate. The proximity of the quantum gas to the surface of the first imaging lens gives rise to a solid immersion effect that allows us to enhance our numerical aperture by a factor of the index of refraction of the glass.

from the first imaging lens (1.1a), limiting the numerical aperture to $NA \approx 1$ which corresponds to a resolution of $5\mu\text{m}$. In addition to suffering from low resolution, imaging a three dimensional BEC in this way necessarily leads to an averaging effect along the imaging axis when a two dimensional image is produced [49]. A slicing procedure must be employed in order for single site information to not be lost [64, 4]. We solve these problems by first increasing the numerical aperture of the imaging system. This allows us to achieve the resolution we require while at the same time shrinking the depth of focus of the imaging system such that only a single lattice plane is in focus at a given time. We then create a 2D quantum gas and load it into a single plane of the lattice allowing us to image the entire 2D quantum gas in a single

exposure with no out of focus background or averaging effects.

The imaging setup consists of a long working distance microscope objective which sits very close to the atoms but remains outside of the vacuum chamber, together with an in vacuum hemispheric optic. The hemispheric optic is a custom design and facilitates both the production of evanescent wave potentials as well as an enhanced imaging resolution due to a solid immersion effect that we are able to exploit due to the proximity of the atoms to the flat side of the hemisphere. The combination of the microscope objective together with the hemispheric front lens allows us to achieve a very large numerical aperture of $NA=0.8$, corresponding to a diffraction limited resolution of $\approx 500\text{nm}$.

To realize the benefits of our high resolution system we create a 2D quantum gas and load it into a single plane of a one dimensional optical lattice potential. By creating a 2D quantum gas with a healing length along the imaging axis much longer than the size of the sample, we eliminate any averaging effects during the imaging process. Furthermore, by loading the 2D quantum gas into a single plane of an optical lattice we eliminate all out of focus background that would otherwise be collected from adjacent lattice planes.

We create the 2D confinement for the BEC by implementing a novel hybrid surface trap [31] that combines magnetic fields, evanescent waves, and standing waves. The magnetic fields are created by a group of coils that sit outside of the vacuum chamber. Evanescent wave potentials are created by blue detuned laser beams incident upon the planar facets of the hemisphere and then totally internally reflected from the glass-vacuum interface that forms bottom side of the hemisphere. Standing wave potentials

are created by reflecting a laser beam off of the bottom face of the hemisphere, creating a standing wave in the vertical direction. By combining magnetic and evanescent wave potentials we realize a 2D confinement for the atoms with long lifetimes just a few microns away from the glass surface. We then load the atoms directly into a single well of a one dimensional standing wave, which allows us to achieve an even stronger vertical confinement. The stronger confinement takes us deeper into the 2D regime allowing us to reach aspect ratios of 300:1:1.

With the 2D quantum gas loaded into a single plane of an optical lattice potential, we add periodic potentials in the other two dimensions to realize a model system for condensed matter physics. In this experiment, our high numerical aperture setup facilitates the creation of optical lattice potentials by using the imaging system in reverse. We holographically project periodic phase patterns onto the atoms, creating 2D lattice potentials in the plane. The periodicity and geometry of the 2D lattice potentials in the plane can be controlled exclusively by pattern of the holographic phase mask. The technique of holographic projection is not limited to periodic potentials though. Arbitrary potential landscapes can be created and projected onto the atoms by choosing the appropriate phase mask, making this a very powerful and flexible tool for the creation of complex many body systems.

After adding a 2D lattice potential in the plane, we make use of the high resolution imaging system. Ramping up a very deep near detuned lattice that pins the atoms in place, we illuminate the atoms with an optical molasses [59] that simultaneously cools the atoms while they scatter photons that are collected by the imaging optics. This technique allows us to collect fluorescence photons indefinitely (only limited by

vacuum lifetime), allowing us to obtain a signal with very high fidelity.

To realize maximally smooth optical potentials for both the creation of the 2D conservative lattice as well as the evanescent wave and standing wave, we demonstrate for the first time the use of broadband laser light for the trapping and manipulation of ultra cold atoms. Using broadband light may seem like a very strange idea at first glance, but the reality is that the temporal coherence of lasers used for creating dipole potentials is often much more than needed and may in fact be harmful. We minimize any unwanted interferences in the system by using broadband light with a short coherence length of around $150\mu\text{m}$. Stray light at the position of the atoms no longer interferes coherently as long as it travels more than a coherence length before returning to the atoms.

1.4 Organization of this thesis

This thesis is organized as follows:

- Chapter 2 is a brief summary of theory relevant to this experiment.
- Chapter 3 describes the parts of the apparatus necessary for creating BEC as well as our basic production sequence.
- Chapter 4 is a description of the magnetic fields used to control the atom position throughout the experiment.
- Chapter 5 is a summary of the construction and realization of the evanescent wave surface trap

- Chapter 6 describes the completion of our 2D hybrid surface trap
- Chapter 7 is a description of our novel imaging system and also presents some the first results from the quantum gas microscope.

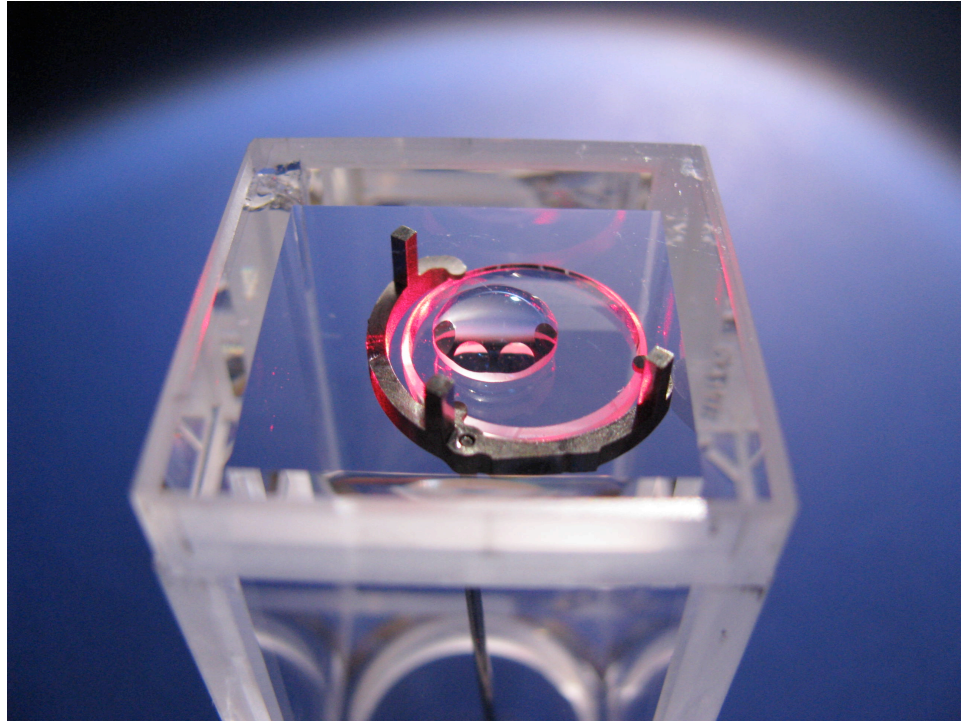


Figure 1.2: Hemisphere used to create evanescent wave surface trap as well as provide enhanced imaging resolution via a solid immersion effect, it is the centerpiece of the apparatus. The bevels mimic a prism like structure for the entry of laser beams that create the evanescent wave potential.

Chapter 2

Theory

2.1 Bose-Einstein condensates

2.1.1 Intro

Bose-Einstein condensation (BEC) was predicted by Einstein in 1924 [25], closely following the new work of Bose [12]. BEC occurs in an ideal gas of bosonic atoms when the thermal de Broglie wavelength

$$\lambda_{dB} = \frac{h}{\sqrt{2\pi mk_B T}} \quad (2.1)$$

becomes comparable to the interparticle spacing [66]. The overlapping wave functions give rise to a macroscopically occupied ground state of the trapping potential.

2.1.2 Dimensionality

The BEC transition temperature in a non-interacting Bose gas can be found from the expression [66]

$$N = \int_0^\infty g(\epsilon)f(\epsilon) d\epsilon \quad (2.2)$$

where $f(\epsilon)$ is the Bose distribution function [12] with the chemical potential set to $\mu=0$, $g(\epsilon)$ is the density of states, and N is the total number of particles. Integrating and solving for the critical temperature T_c we find that in free space ($g(\epsilon) \propto \epsilon^{d/2-1}$) there is no finite temperature phase transition below three dimensions. However, in the presence of a harmonic trapping potential the density of states is modified ($g(\epsilon) \propto \epsilon^{d-1}$) and the situation is qualitatively different. Inserting the density of states for a harmonic trapping potential into equation 2.2 we find that for the two and three dimensional cases there is a finite temperature phase transition given by

$$k_b T_c = \frac{\hbar \bar{\omega} N^{1/\alpha}}{\zeta(d)^{1/\alpha}} \quad (2.3)$$

where $\zeta(d)$ is the Riemann-Zeta function, $\bar{\omega}$ is the geometric mean of the trapping frequencies, and d is the dimensionality of the system. While condensation is predicted to occur in this instance, it has been pointed out in [11] that non-interacting BEC in a 2D harmonic trapping potential is very fragile. In light of this observation, we will focus our attention on the more relevant case of repulsive interactions.

2.1.3 Interacting BEC

For all discussions in this thesis, we will assume a harmonic trapping potential of the form $V_{ext}(\mathbf{r}) = \frac{1}{2}m(\omega_1^2 x^2 + \omega_2^2 y^2 + \omega_3^2 z^2)$. In order to properly take interactions into account when describing the ground state wave function of the condensate, we must turn to the Gross-Pitaevskii equation. The Gross-Pitaevskii equation describes

the condensate wave function in the limit that the s-wave scattering length a is much smaller than the particle separation, $n|a|^3 \ll 1$, where n is the density of the atomic gas. The s-wave scattering length in ^{87}Rb is $\approx 5\text{nm}$ which is much smaller than the smallest particle separation ever reported in cold alkali vapor ($10^{14}/\text{cm}^3$) [22]. In this limit we can approximate the complicated interatomic potential with a contact interaction of the form $g\delta(\mathbf{r},\mathbf{r}')$ with $g = \frac{4\pi\hbar^2 a}{m}$, where m is the atomic mass. The time independent Gross-Pitaevskii equation [40, 70] then yields

$$\mu\phi(\mathbf{r}) = \left(-\frac{\hbar^2}{2m}\nabla^2 + V_{ext}(\mathbf{r}) + g|\phi(\mathbf{r})|^2 \right) \phi(\mathbf{r}) \quad (2.4)$$

where μ is the chemical potential and $g|\phi(\mathbf{r})|^2$ is the mean field interaction. This equation is difficult to solve in general but can be simplified under certain circumstances.

2.1.4 Thomas-Fermi approximation

For large atom numbers and repulsive interactions, which is always the case in our experiments performed with ^{87}Rb , we may simply neglect the kinetic term in equation 2.4, yielding $\mu = V_{ext}(\mathbf{r}) + gn(\mathbf{r})$, where we have used the fact that $n(\mathbf{r}) = \phi^2(\mathbf{r})$. This equation gives the form of the in-trap density of the condensate to be

$$n(\mathbf{r}) = \frac{\mu - V_{ext}(\mathbf{r})}{g} \text{ for } \mu - V_{ext}(\mathbf{r}) > 0 \quad (2.5)$$

describing a parabolic density profile in the trap where the atoms fill up the trap to a height of the chemical potential. This parabolic profile is maintained even after a time of flight due to the effect of interactions as the cloud expands [14, 48]. The

Thomas-Fermi approximation [21] allows us to calculate both the cloud radius and chemical potential as

$$R_i = \sqrt{\frac{2\mu}{m\omega_i^2}} \quad (2.6)$$

$$\mu_{3D} = \frac{15^{2/5}}{2} \left(\frac{Na}{\bar{a}} \right)^{2/5} \hbar\bar{\omega} \quad (2.7)$$

where \bar{a} is the geometric mean of the oscillator lengths and $\bar{\omega}$ is the geometric mean of the trapping frequencies.

2.1.5 Dimensionality revisited

The theory of interacting BEC in two dimensions is rather involved [67, 68] and so only a brief summary of the aspects important to this experiment will be included. For a 2D interacting quantum gas there is a phase transition at the critical temperature T_C to a macroscopically occupied ground state which manifests itself as a bimodal distribution in the weakly confined directions and a Gaussian distribution in the tightly confining direction. There is much more to the story, however. Unlike the situation in three dimensions, at the BEC transition temperature in two dimensions there is not a uniform phase throughout the sample, but rather there are patches of uniform phase with the patch size being larger than the healing length of the cloud, but smaller than the size of the sample.

The lack of uniformity in the phase across the condensate is due to unbound vortices which are present in the condensate at temperatures above the Berezinskii-Kosterlitz-Thouless (BKT) transition temperature [7, 53]. Below the BKT transition

temperature, the vortices exist only in bound pairs and hence they no longer affect the spatial phase coherence of the BEC. Clearly, since we are interested in loading a 2D BEC into an optical lattice, we need to be able to control the temperature of the sample in order to ensure that we can "freeze" the vortices out of the system. Once the vortices are frozen out, there remain long wavelength phase fluctuations in the system but these long wavelength fluctuations have not been an impediment in previous experiments [79, 29].

The BKT transition temperature is universal and given by the expression [61] $n_s \lambda_T^2 = 4$, where n_s is the superfluid density and λ_T is the thermal de Broglie wavelength. In experiments, we measure the total density of the sample and thus need to relate the total density to the superfluid fraction. For weak interactions, the total density at the transition point can be calculated via Monte Carlo calculations [71] as $n \lambda_T^2 = \ln(C/\tilde{g})$ with $C=380 \pm 3$ and the dimensionless parameter $\tilde{g} = \sqrt{8\pi} a/l_z$ given by the ratio of the s-wave scattering length and the harmonic oscillator length in the tightly confining dimension. Calculating the ratio of the two transition temperatures for our particular trapping configuration, we find that $T_{BKT}/T_{BEC} \approx .46$. Experimentally, this means that we must have excellent control over the temperature in the 2D trap in order to be able to cool the sample sufficiently below T_{BKT} such that it is free of unbound vortices. A recent paper by the NIST group has investigated this hierarchy of temperature scales in a 2D Bose gas of sodium atoms [17].

2.1.6 2D Bose condensation

We live in a three dimensional world and so do most BECs. Taking a BEC into the 2D regime requires that we kinematically freeze out one of the dimensions [32] by making one of the trapping frequencies so large that the energy spacing between adjacent harmonic oscillator levels is much larger than any other energy scale in the system, $\hbar\omega \gg \mu_{3D}, k_bT$. In most experiments $\mu_{3D} > k_bT$, so the inequality is usually written as $\hbar\omega \gg \mu_{3D}$. Alternatively, we can consider length scales instead of energy scales. A system enters the 2D regime when the healing length (correlation length) given by $\xi = (4\pi na)^{-1/2}$ becomes larger than the harmonic oscillator length along the tightly confining dimension, $\xi \gg x_{ho}$.

2.2 Optical lattices

2.2.1 Optical potentials

Optical dipole potentials have been used for quite some time in atomic physics to manipulate and trap neutral atoms [16, 9] via both conservative and dissipative forces. A light field incident upon a neutral atom induces an electric dipole moment given by [44] $d = \alpha(\omega)E$ where $\alpha(\omega)$ is the complex polarizability, E is the incident electric field, and ω is the frequency of the incident light field. This induced electric dipole moment then interacts with the incident electric field, leading to a conservative interaction potential of the form $V_{dip} = -\frac{1}{2}\langle d \cdot E \rangle$. The laser-atom interaction also gives rise to a dissipative force that results from the absorption and spontaneous re-emission of photons, in contrast with the conservative dipole force that results from

a shift in potential energy or AC-Stark shift. The dissipative force is often quantified in terms of the spontaneous scattering rate which is given by $\Gamma_{sc} = \frac{1}{\hbar\omega} \langle \dot{d} \cdot E \rangle$.

Optical lattice experiments are typically performed with atoms in the nanokelvin regime and as such require potentials that are conservative on the time scale of typical experiments which are on the order of a few seconds. Since the strength of the conservative potential goes down as $1/\delta$ and the scattering rate goes down as $1/\delta^2$, we can minimize the scattering rate by choosing δ the laser detuning to be as large as the laser power allows. For a two-level atom, the conservative dipole potential and spontaneous scattering rate are given by

$$V_{dipole}(\mathbf{r}) = \frac{3\pi c^2}{2\omega_0^3} \left(\frac{\Gamma}{\omega_0 - \omega} + \frac{\Gamma}{\omega_0 + \omega} \right) I(\mathbf{r}) \approx \frac{3\pi c^2}{2\omega_0^3} \times \frac{\Gamma}{\Delta} I(\mathbf{r}) \quad (2.8)$$

$$\Gamma_{sc}(\mathbf{r}) = \frac{3\pi c^2}{2\hbar\omega_0^3} \left(\frac{\omega}{\omega_0} \right)^3 \left(\frac{\Gamma}{\omega_0 - \omega} + \frac{\Gamma}{\omega_0 + \omega} \right) I(\mathbf{r}) \approx \frac{3\pi c^2}{2\hbar\omega_0^3} \times \frac{\Gamma^2}{\Delta^2} I(\mathbf{r}) \quad (2.9)$$

where $\Delta = \omega_0 - \omega$ and the rotating wave approximation has been used to obtain the approximate expressions on the right hand side. In our experiments with ^{87}Rb we do not always work in a regime where we can make the simple two level approximation. A more general expression for the dipole potential that takes into account the multiple energy levels is [38]

$$V_{dipole}(\mathbf{r}) = \frac{\pi c^2 \Gamma}{2\omega_0^3} \left(\frac{2 + P g_F m_F}{\Delta_{2,F}} + \frac{1 - P g_F m_F}{\Delta_{1,F}} \right) I(\mathbf{r}) \quad (2.10)$$

which can be used so long as Δ is large compared with the excited state hyperfine splitting. Here P is ± 1 or 0 for $\sigma\pm$ or linear light respectively and $\Delta_{j,F}$ is the detuning from the D1 or D2 line.

2.2.2 Gaussian beams

The spatially varying profile of a Gaussian beam gives rise to a potential that can be used to create confinement for neutral atoms. A Gaussian beam has a profile given by

$$I(r, z) = \frac{P}{\pi w^2(z)} e^{-\frac{2r^2}{w^2(z)}} \quad (2.11)$$

where $w(z) = w_0 \sqrt{1 + (\frac{z}{z_R})^2}$ is the $1/e^2$ radius, P is the power in the beam, and $z_R = \pi w_0^2 / \lambda$ is the Rayleigh length. For a red detuned laser beam, the Gaussian profile will give rise to a trapping potential with trap frequencies near the trap center given by

$$\omega_r = \sqrt{\frac{4V_0}{mw_0^2}} \quad (2.12)$$

$$\omega_z = \sqrt{\frac{2V_0}{mz_R^2}} \quad (2.13)$$

where V_0 is the maximum potential depth and ω_r, ω_z are the radial, axial trapping frequencies respectively.

2.2.3 Periodic optical potentials

In this thesis we are rarely interested in the confinement from the Gaussian profile of the laser beams, rather we are interested in using laser beams to create optical lattice potentials that are periodic in space. The simplest periodic potential that we can create to trap ultra cold atoms is a one-dimensional standing wave. A one dimensional standing wave is formed by two counter propagating laser beams, creating

a periodic potential to confine the atoms. To create higher dimensional confinement, we need only add additional pairs of beams. In this way, we can construct one, two, and three dimensional optical lattice potentials.

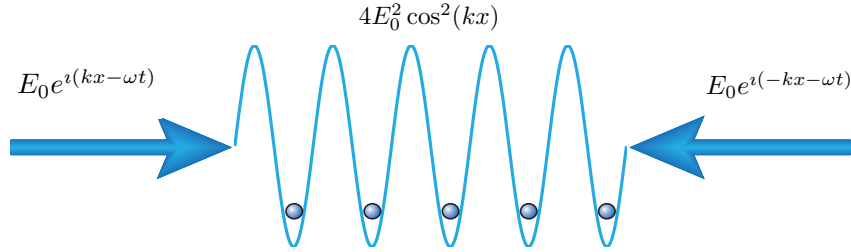


Figure 2.1: Two counterpropagating laser beams form a one dimensional standing wave. Atoms are trapped in the potential minima created by the resultant interference pattern. Note that there is a factor of 4 enhancement in the intensity due to the interference of the light.

In this experiment we use slight variations of the counterpropagating beam configuration to make our lattices as shown in figure 2.2.

For a 1D standing wave such as that in figure 2.1, if we approximate each atom as sitting in the bottom of a harmonic well we find an expression for the trapping frequency in the lattice as

$$\omega_x = \sqrt{\frac{V_{lat} 2k^2}{m}} \quad (2.14)$$

where V_{lat} is the lattice depth.

2.3 Band structure

The signature of a periodic potential is band structure, regardless of the fine details of the periodic potential [37]. The classic study on band structure was performed with

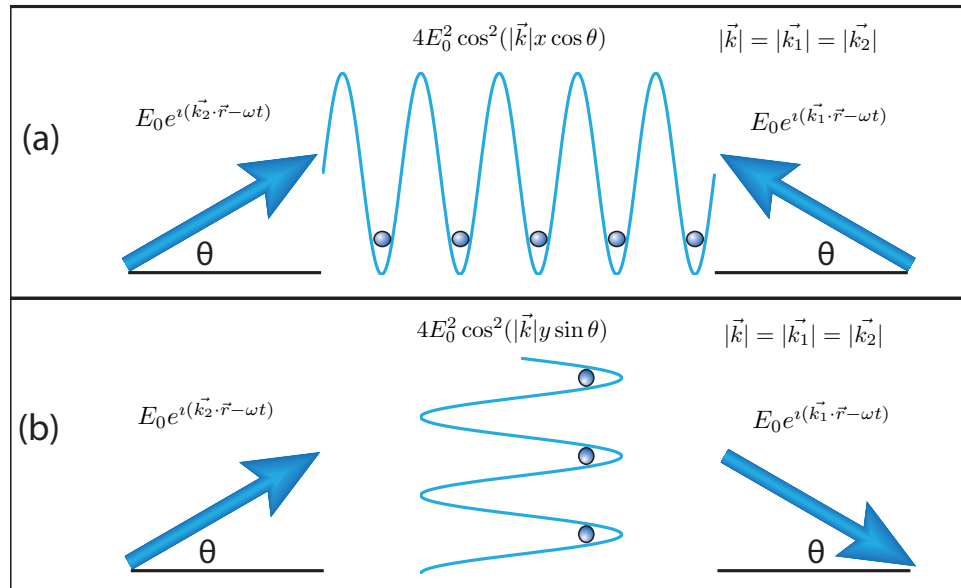


Figure 2.2: In this experiment we do not use counterpropagating laser beams to create our optical lattice potentials. Instead, we use configurations such as those shown in this figure. (a) Standing wave with lattice period $\pi/(k \cdot \cos \theta)$ created by two beams sent from hologram through microscope objective. (b) Standing wave with lattice period $\pi/(k \cdot \sin \theta)$ created from a laser beam after reflecting off of the bottom face of the hemisphere.

a periodic square well potential [54]. For this thesis it is of greater utility to focus on potentials created by laser standing waves, namely sinusoidal periodic potentials. In our experiments performed with ^{87}Rb we use a two dimensional square lattice that provides a separable potential, allowing us to calculate the band structure in each dimension separately.

2.3.1 Bloch's theorem

Given a periodic potential $V(x)$ with a Hamiltonian given by $H = p^2/2m + V(x)$, Bloch's theorem states that the eigenfunctions of the system $\phi_q^{(n)}(x)$ will have the following form

$$\phi_q^{(n)}(x) = e^{\frac{iqx}{\hbar}} \cdot u_q^{(n)}(x) \quad (2.15)$$

where $u_q^{(n)}(x)$ has the same periodicity as $V(x)$, q is the crystal momentum or quasi momentum, and n is the band index. Using the trial wave function given above, we can solve the system to find the structure of the energy levels for a periodic potential of the form $V(x) = V_{latt}(1 - \cos(2kx))$. The details of the calculation can be found in [5].

2.3.2 Wannier functions

For shallow lattices the atoms are completely delocalized and a Bloch wave picture is a good description of the system. For deeper lattices however, the atoms become confined to individual lattice sites and a new basis becomes a more appropriate description of the system. Wannier functions [84] form a basis comprised of functions that are maximally localized and can be calculated as a sum of Bloch waves given by

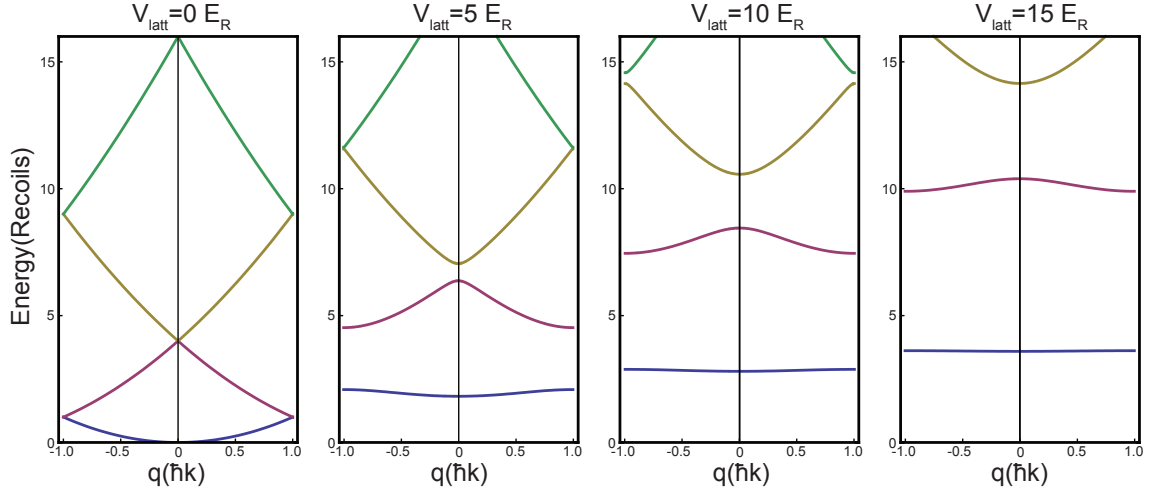


Figure 2.3: Plotted are the energies of the first four Bloch waves as a function of the quasimomentum. The energy is plotted in units of lattice recoils, $E_R = \hbar^2/2m\lambda^2$, while the quasi momentum q is plotted in units of $\hbar k$, with k related to the lattice constant a by $k = \pi/a$.

[51]

$$w_n(x - x_i) = \frac{1}{\sqrt{N}} \sum_q e^{iqx_i/\hbar} \phi_q^n(x) \quad (2.16)$$

where the sum is carried out over the first Brillouin zone, x_i is the position of the i th lattice site, and N is a normalization constant. With the Wannier functions in hand, we are in position to calculate the tunneling rate and on-site interaction terms that will come in handy later. The tunneling rate between adjacent lattice sites can be found as follows ¹

$$J = \int w_n(x - x_i) \left(-\frac{\hbar^2}{2m} \frac{\partial^2}{\partial x^2} + V(x) \right) w_n(x - x_j) dx \quad (2.17)$$

and the onsite interaction between atoms can be found as

$$U = \frac{4\pi\hbar^2 a}{m} \int |w_n(x - x_i) \cdot w_n(y - y_i) \cdot w_n(z - z_i)|^4 d^3\mathbf{x} \quad (2.18)$$

2.4 Bose-Hubbard Hamiltonian

The Hubbard Hamiltonian was originally introduced to describe the transition between conducting and insulating states in solid state systems [43]. The Hubbard description is the simplest many-body Hamiltonian that cannot be reduced to a single particle problem. Ultra cold atoms in the lowest band of an optical lattice are a nearly pure realization of the Hubbard model [45], that had been previously regarded as a "toy" model. The Bose-Hubbard Hamiltonian [28] can be written as follows

$$\hat{H} = -J \sum_{\langle i,j \rangle} \hat{a}_i^\dagger \hat{a}_j + \sum_i (\epsilon_i - \mu) \hat{n}_i + \sum_i \frac{U}{2} \hat{n}_i (\hat{n}_i - 1) \quad (2.19)$$

so that the first term is the kinetic energy term or "hopping" term that describes tunneling between nearest neighbor lattice sites, while the last term is the on-site interaction energy between the atoms. When the kinetic term is dominant over the interaction term ($J \gg U$), the atoms are delocalized over the lattice in a superfluid phase. On the flip side, when the interactions are dominant over the kinetic term ($U \gg J$), the atoms tend to localize, leading to a Mott insulating phase where the atom number on each lattice site takes on well defined integer values. The central term includes both an energy offset ϵ_i and the chemical potential μ .

¹The expression for the tunneling matrix element J is only valid for a separable lattice potential.

2.5 Mott insulator

In an optical lattice system, the ratio of kinetic to interaction energy can be dynamically varied by changing the depth of the lattice potential. In this way it has been possible to observe the Mott Insulator in an optical lattice system with both bosons [35] and fermions [47]. While the ratio of J/U determines when the Mott insulator phase transition occurs, if the absolute value of the tunneling J is small so that the tunneling time is long, then the atoms do not have sufficient time to rearrange themselves on the timescale of the experiment making the Mott insulator inaccessible. In general we need to keep the tunneling times short via small lattice constants so that we have access to many-body physics that results from a competition between the different terms in the Hamiltonian.

Chapter 3

Creation of a Bose-Einstein condensate

3.1 Overview

Our BEC machine is a double chamber design similar to that of Greiner *et al.* [34]. The setup consists of a magneto-optical trap (MOT) [72] and a separate ultra-high vacuum (UHV) region with an attached glass cell which acts as our "science chamber". A gate valve separates the two chambers, allowing components to be interchanged without breaking vacuum. The setup is optimized to provide maximum optical access to the atoms sitting inside of the glass cell. We magnetically transport the atoms approximately half a meter from the MOT chamber to the glass cell before loading them into a quadrupole Ioffe-Pritchard configuration (QUIC) trap [27] and performing forced RF evaporation [50]. Approximately every 40 seconds we create BECs in the $|F = 1, m_F = -1\rangle$ state with $2 \cdot 10^5$ atoms.

3.2 Laser setup

Our laser system for the production of BEC is shown in figure 3.1. It consists of two home built external cavity diode lasers [74], one tuned to the cooling transition $|5S_{1/2}, F = 2\rangle \rightarrow |5P_{3/2}, F = 3\rangle$ and one tuned to the repump transition $|5S_{1/2}, F = 1\rangle \rightarrow |5P_{3/2}, F = 2\rangle$ of ^{87}Rb . Both lasers are frequency stabilized to their respective crossover transitions via radiofrequency (RF) spectroscopy [10]. Acousto-optic modulators (AOM) are used to vary the laser frequency about the lock point. Since the cooling laser light is used to perform absorption imaging we do not modulate the laser diode directly (which would add unwanted sidebands). Instead, we split off a small amount of light from the cooling laser and use an electro-optic modulator (EOM) to add RF sidebands directly to the laser beam. This technique ensures that the light used for absorption imaging is free of off-resonant light from the locking procedure.

3.3 Vacuum chamber

The vacuum chamber is pictured in figure 3.2. The MOT chamber is octagonal and flat in order to allow for the transport coils to be placed as close as possible to the atoms. Six windows (MDC 450020) with a large diameter of 35mm allow passage of the laser beams that form the MOT. Directly above the MOT chamber is a reservoir of Rb^{87} that creates a background vapor in the MOT chamber from which we directly load our MOT. Directly below the MOT chamber is an ion pump (Varian 9191340) with a viewport shutter (MDC 454001) that allows us to control the pumping speed

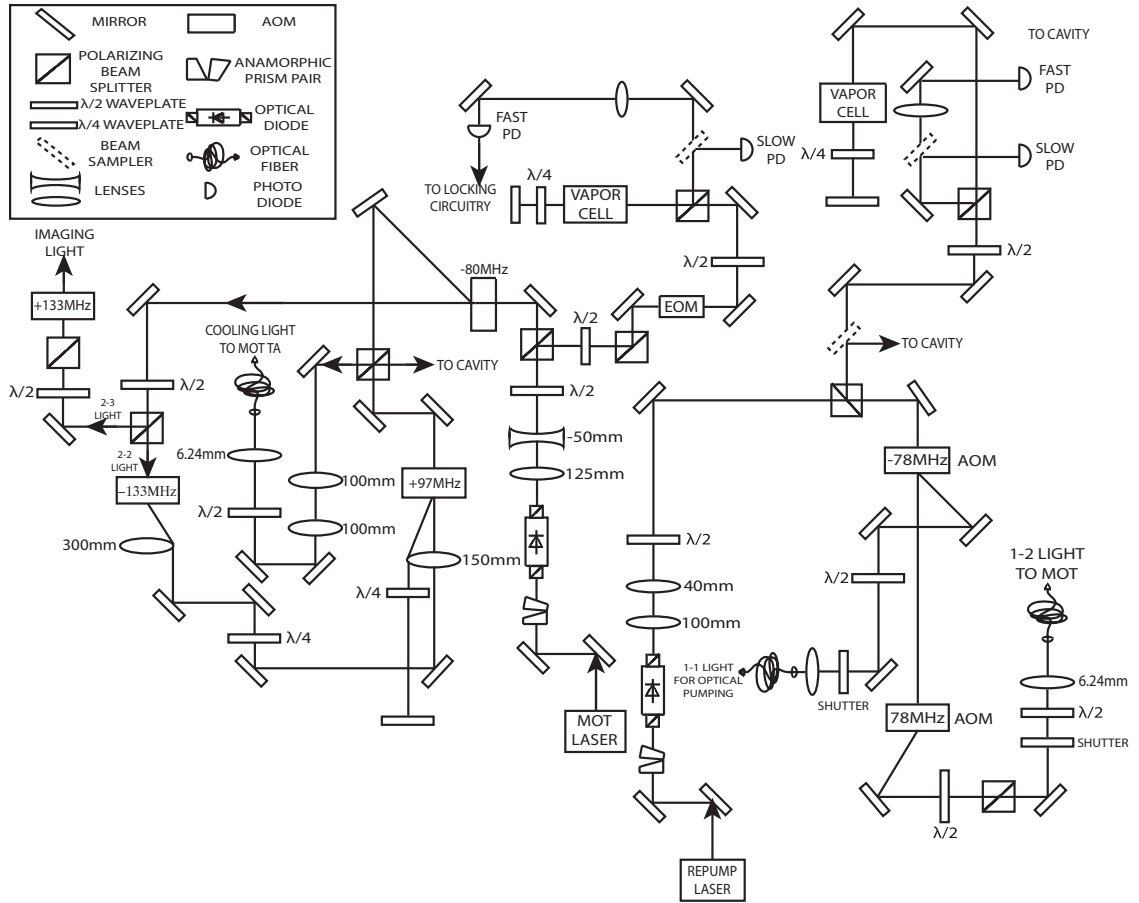


Figure 3.1: Laser setup for BEC production. The MOT laser produces light on the $F = 2 \rightarrow F'$ while the repumper produces light on the $F = 1 \rightarrow F'$.

of the ion pump.

The MOT chamber is operated at a pressure of $4 \cdot 10^{-9}$ Torr while the UHV chamber is operated at pressures less than $2 \cdot 10^{-11}$ Torr. A differential pumping tube with an inner diameter of 8mm and a length of 70mm placed between the MOT and UHV chambers decouples the pressures allowing us to maintain the large pressure difference. An all-metal CF16 gate valve (VAT 48124-CE01-X) allows us to isolate the MOT and UHV chambers allowing them to be modified independently. A five-way cross attached to the UHV chamber allows for the attachment of an

ion pump, ion gauge, titanium sublimation cartridge, and turbo pump on the UHV side. In our setup, turbo pumps are only used during the initial bakeout of the chamber and are subsequently removed, leaving only the ion pumps to maintain the vacuum. The assembly directly below the UHV chamber is separated from the main chamber by an all-metal CF40 gate valve (VAT 48132-CE01-X). The assembly allows us to insert custom optics into the glass cell via a translation stage (UHV Design HLSML38-440-H and PA-35) with a stroke of 440mm. The gate valve allows us to independently bake out and pump down the bellows region below the UHV chamber. In this way, we can exchange optics in and out of the glass cell without having to break vacuum in the UHV region. A glass cell attached directly above the UHV chamber serves as our science chamber where the BEC is created and all subsequent parts of the experiment take place. The glass cell is made of fused silica and is anti-reflection coated to minimize stray reflections. Through a diffusion bonding process, the wavefront distortion on all faces of the cell is kept lower than $\frac{\lambda}{10}$. The dimensions of the glass cell are 26mmx26mmx100mm.

3.4 Assembly and bakeout procedure

We inspect each part for damage/contamination upon arrival with special attention paid to the knife edges of the conflat flanges. On at least one occasion we have received a damaged knife edge right out of the box. We have also encountered a few new parts with large oil splotches on them. We clean all of our parts in an ultrasonic bath of soapy water, water, acetone, methanol, and isopropanol, in that order. Any part with excessive oil on it is pre-cleaned with trichloroethylene (TCE should

only be used for special cases as it has been shown to be a potent carcinogen). We bake our chamber by first attaching temperature probes and wrapping it in thick aluminum foil to ensure an even heating throughout the vacuum system. We then place heater tape around the chamber as well as a final aluminum foil layer that is loosely wrapped to keep in the heat. A turbo pump is attached to the chamber and turned on throughout the duration of the bake out. We employ a simple feedback loop to control the temperature of the chamber and in this way we can slowly ramp up the temperature of the chamber to avoid any excessive thermal gradients.

We bake most of our chamber to 200C for a few days until the pressure drops to $1 \cdot 10^{-7}$ Torr. During this time, the ion pumps are switched off and only the turbo pump is energized. We cool it down slowly, reaching a pressure of roughly $1 \cdot 10^{-10}$ Torr. We then turn on the ion pumps while the turbo pump is still running. We wait for any contaminants released by the ion pump to be pumped out of the system before isolating the turbo pump from the system by closing the isolation valve. Once the isolation valve is closed the system no longer has any open paths to the atmosphere making the system invulnerable to power outages. To reach the pressures required for RF evaporation, we fire our titanium sublimation pump by pulsing on a current of 47 Amps through one of the filaments for 1 minute. In this way, we are able to reach pressures of $< 2 \cdot 10^{-11}$ Torr.

3.5 Magneto-optical trap

We operate a vapor cell MOT [1, 69] with a 5 gram sample of rubidium (Alfa Aesar 10315) acting as our reservoir. Our magneto-optical trap is created by six intersecting

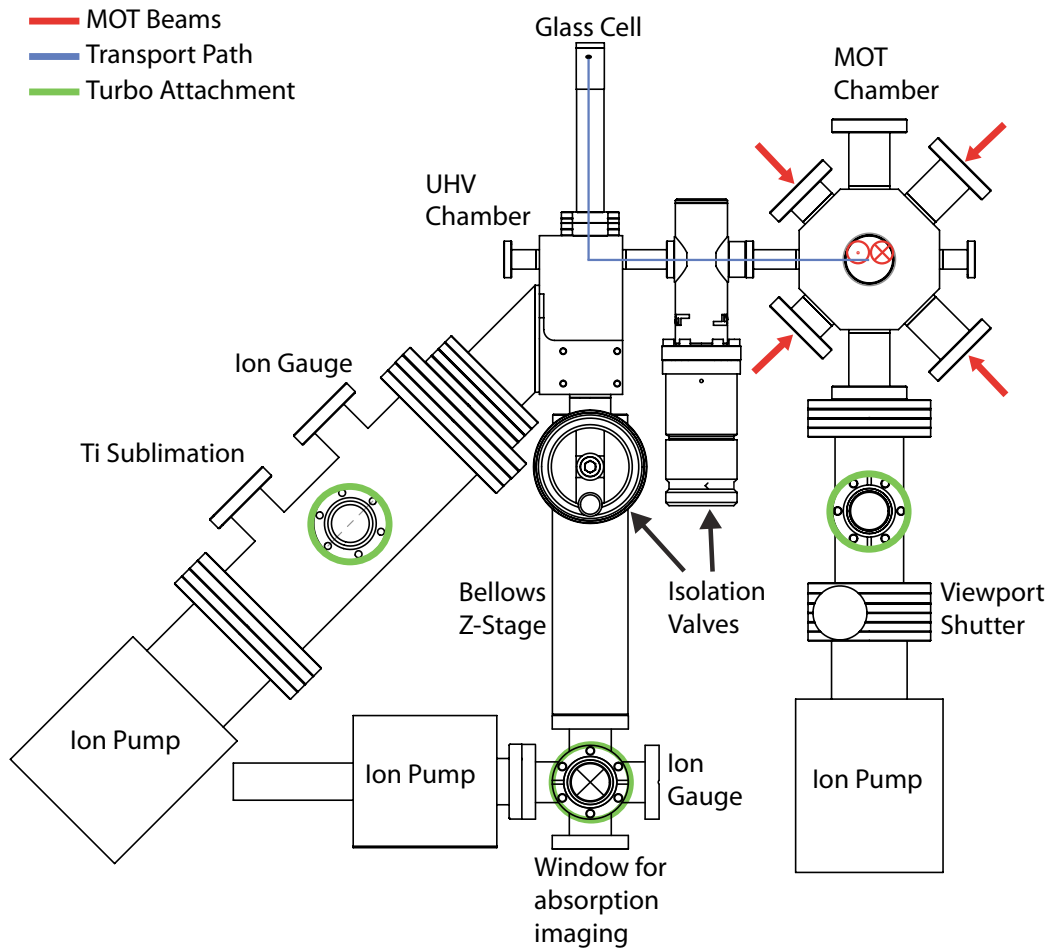


Figure 3.2: Schematic of our vacuum chamber design.

laser beams together with a pair of coils operated in the anti-helmholtz configuration. The laser beams are detuned by -3Γ from the cooling transition with a power of $\approx 30\text{mW}$ per beam. The coils are operated at a modest current of 5 amps, corresponding to a gradient of $\approx 10\text{G/cm}$. We load the MOT for approximately 8 seconds, collecting roughly $1 \cdot 10^9$ atoms at a temperature of $100\mu\text{K}$. After a compression and optical molasses stage, the temperature is reduced to about $40\mu\text{K}$.

3.6 Magnetic transport

Following the loading of the MOT, the atoms are transported to the glass cell in the UHV region where we perform forced RF evaporation. We transport the atoms magnetically using a series of quadrupole coils [34] that smoothly shift the position of the atoms over the half meter distance separating the MOT from the final position of the atoms in the glass cell. Our transport of the atoms differs from the norm because in the second leg of the transport, we transport the atoms vertically upward against gravity. It is for this reason that we require stronger gradients than usual during the final stages of the transport sequence.

3.7 RF evaporation

After the atoms arrive in the glass cell, the trap configuration is changed smoothly from a quadrupole confinement to harmonic confinement with a non-zero offset. A non-zero offset is necessary to avoid majorana losses [56] during the evaporation process. For our evaporation we use a coil close to the atoms that is driven with 2 watts of RF power. As our RF source, we use the Tabor WW5061 function generator which is capable of phase continuous frequency sweeps.

3.8 BEC production sequence

The experimental sequence to create nearly pure Bose-Einstein condensates is shown in figure 3.3. We begin by loading our MOT for 8 seconds, followed by a compression and molasses phase. We then optically pump the atoms to the $|F =$

$|1, m_F = -1\rangle$ to maximize the number of atoms captured in the magnetic trap. After loading the atoms into the magnetic trap, we shine in a resonant beam that removes any atoms in the $F=2$ ground state. We then transport the atoms to the glass cell by smoothly ramping the transport coils. After the atoms arrive at the glass cell, we ramp up the quadrupole confinement before smoothly changing to a QUIC trap with a cigar-type confinement. We perform forced RF evaporation to achieve quantum degeneracy. We produce nearly pure BECs in the $|F = 1, m_F = -1\rangle$ state with a typical number of atoms being $2 \cdot 10^5$. After production of the BEC, we slowly raise the offset field in the QUIC trap to achieve a nearly spherical confinement.

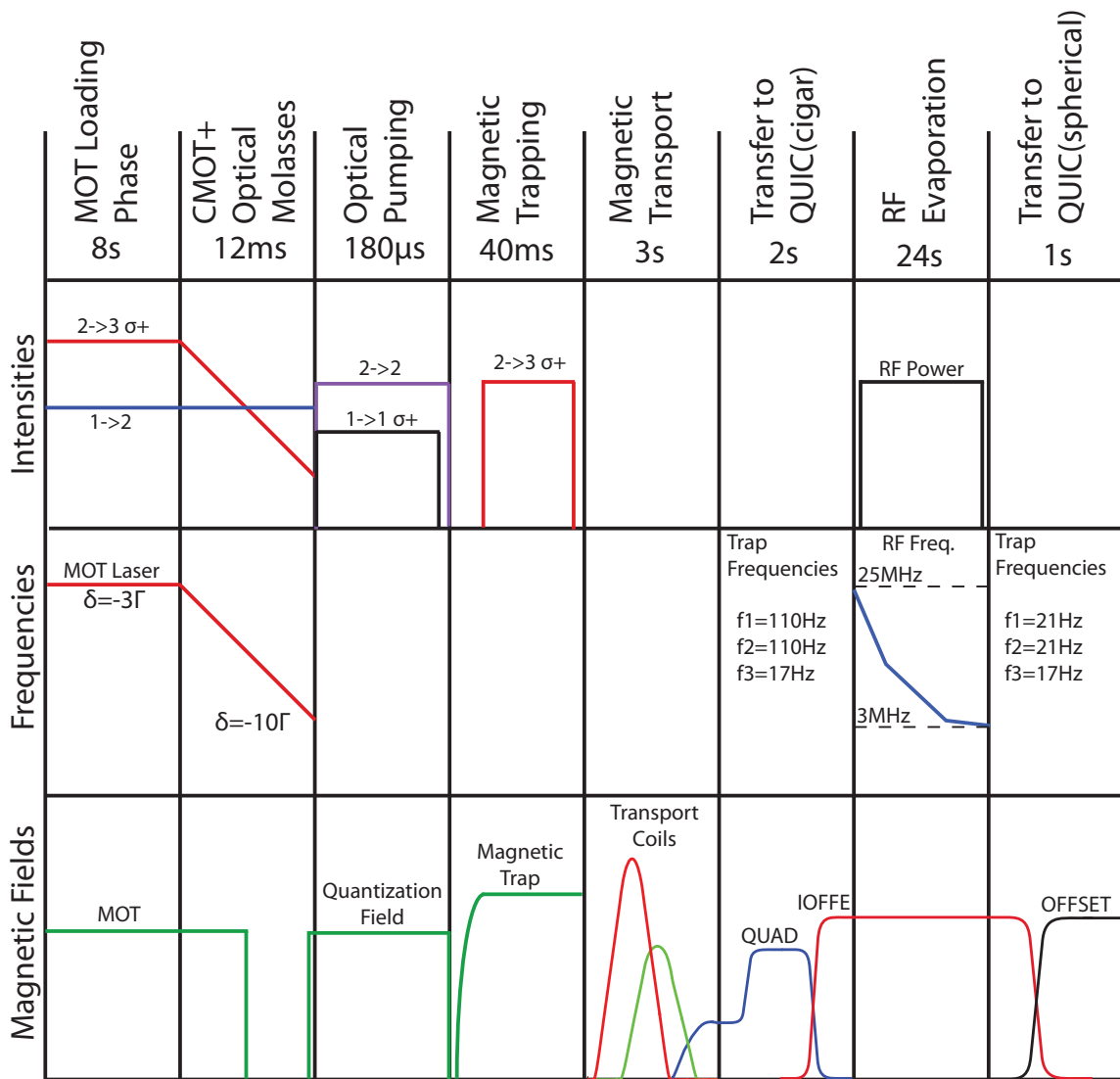


Figure 3.3: Overview of BEC production sequence.

Chapter 4

Magnetic field control

4.1 Introduction

Magnetic fields are central to this experiment. Beginning with the MOT and ending with the transfer of atoms into a two dimensional optical lattice, magnetic fields provide us with the ability to control the position of the atoms throughout the experiment in a very clean and reproducible way.

4.2 Magnetic trapping of neutral atoms

The potential energy of a neutral atom in a magnetic field has the form $U_{magnetic} = -\boldsymbol{\mu} \cdot \mathbf{B}$. If the external magnetic field is small compared to the hyperfine ground state splitting which in this case is 6.8GHz for ^{87}Rb , then \mathbf{F} is a good quantum number and we can write the energy of the atom as $E_{magnetic} = \mu_B m_F g_F B$ where μ_B is the Bohr magneton, m_F is the angular momentum quantum number in the z direction,

and g_F is Lande's g factor. Since it is not possible to create a static maximum in the external magnetic confinement by Maxwell's equations, we instead create a magnetic field minimum to trap the atoms. This of course limits our choice of magnetic spin states, which for Rb^{87} means that we can trap only the weak field seeking states, $|F = 2, m_F = +2\rangle$, $|F = 2, m_F = +1\rangle$, and $|F = 1, m_F = -1\rangle$. The atomic magnetic moment precesses in the external magnetic field with a Larmor precession frequency of $\omega_L = \mu_B m_F g_F B / \hbar$. As long as the external magnetic confinement is changing slowly compared with the Larmor frequency, then the atomic spin will follow the external field and the spin state will be preserved.

4.3 Quadrupole traps

A quadrupole trapping potential can be formed by placing two coils in the same orientation, but spaced apart from one another and with equal and opposite currents. This is called the anti-helmoltz configuration. Currents in opposite directions are sent through the two coils, creating a linear potential in all directions near the center of the two coils with $B(\mathbf{r}) = \alpha x \hat{x} + \beta y \hat{y} + \gamma z \hat{z}$. For circular coils with their axes aligned along z , $\alpha = \beta$ and by taking note that $\nabla \cdot \mathbf{B} = 0$ we also arrive at the constraint that $\gamma = -2\alpha$. Putting this all together, we arrive at the expression $B(\mathbf{r}) = \alpha x \hat{x} + \alpha y \hat{y} - 2\alpha z \hat{z}$. Quadrupole potentials do very well for trapping and manipulating atomic samples at $10\mu\text{K}$ and above. However, below this temperature they begin to suffer from Majorana losses. As the atomic sample gets colder, the atoms spend more time near the center of the trap where the magnetic field becomes arbitrarily small. Eventually the atoms are not able to adiabatically follow the magnetic field because the Larmor

frequency becomes vanishingly small. When this happens the atoms can flip their spin and become anti-trapped and lost. It is for this reason that we need to use a magnetic trapping potential with a non zero minimum during the forced RF evaporation prior to achieving BEC.

4.4 Magnetic transport

While quadrupole potentials may not be suitable for RF evaporation, they are particularly well suited to magnetically transport atoms through large distances. For our magnetic transport from the MOT chamber to the glass cell, we employ 13 quadrupole pairs and one push coil. The atoms begin their journey in the MOT and after traveling 452.5mm within a few seconds, they arrive at the glass cell ready to be loaded into the QUIC trap for RF evaporation.

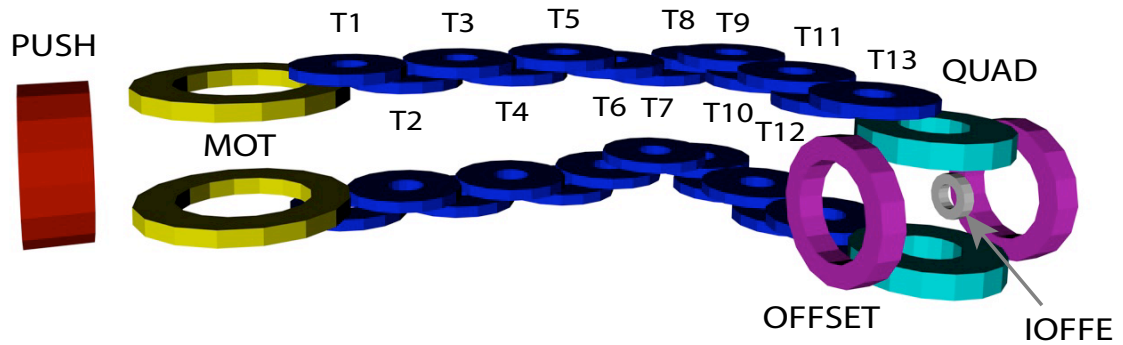


Figure 4.1: Schematic of the coils used for the magnetic transport. T1-T13 and PUSH are used to transport the atoms from the MOT chamber to the glass cell. QUAD, IOFFE, and OFFSET constitute the coils used to implement our QUIC trap.

4.4.1 Calculation of currents

Transporting atoms from the MOT chamber to the glass cell requires the use of 15 independent quadrupole pairs and one push coil near the MOT chamber. To transport the atoms with minimal heating, we make sure that the atom position changes smoothly during the transport process. Additionally, we need to minimize aspect ratio changes in the quadrupole trapping potential. Energizing only three coil pairs at a time, we are able to smoothly shift the position of the atoms while minimizing changes in the shape of the trapping potential. We calculate the currents in the coils as a function of position by enforcing three independent constraints as shown below.

$$I_1 B_1(x, 0, 0) + I_2 B_2(x, 0, 0) + I_3 B_3(x, 0, 0) = 0 \quad (4.1)$$

$$I_1 \frac{\partial B_1(x, 0, 0)}{\partial x} + I_2 \frac{\partial B_2(x, 0, 0)}{\partial x} + I_3 \frac{\partial B_3(x, 0, 0)}{\partial x} = \textit{Gradient} \quad (4.2)$$

$$\frac{I_1 \frac{\partial B_1(x, 0, 0)}{\partial x} + I_2 \frac{\partial B_2(x, 0, 0)}{\partial x} + I_3 \frac{\partial B_3(x, 0, 0)}{\partial x}}{I_1 \frac{\partial B_1(x, 0, 0)}{\partial y} + I_2 \frac{\partial B_2(x, 0, 0)}{\partial y} + I_3 \frac{\partial B_3(x, 0, 0)}{\partial y}} = \textit{AspectRatio} \quad (4.3)$$

Figure 4.2: Constraint equations for determining the currents used to generate the magnetic fields that transport the atoms. Equation 4.1 determines the position of the atom cloud as a function of the position x , defined to be along the direction of transport; equation 4.2 constrains the gradient of the magnetic field along the x axis; equation 4.3 constrains the ratio of the gradients in the x and y direction, which allows us to transport the atoms with minimal changes in the trap shape to minimize heating of the atom cloud. Note that in the above formulation, the z axis is the symmetry axis of the quadrupole pair.

4.4.2 Circuitry for magnetic field control

In our experiment, we use a limited number of power supplies (Delta Elektronika SM15-100, SM26-60) during the magnetic transport, meaning that these power supplies must be shared amongst all of the coils during the transport process. Each coil is connected to one of the power supplies via a MOSFET (Microsemi APTM20DUM04G, IXYS IXFN180N20), that when energized allows current to be driven through the coil. A circuit diagram for the magnetic field control is shown in figure 4.3. Varistors are placed across the source to drain connection on each MOSFET to limit any voltage spikes occurring during switchoff. Diodes are placed in series with each coil to prevent current flow in the wrong direction.

4.4.3 Physical design of coils

The coils for the magnetic transport are wound from kapton insulated rectangular copper wire and encapsulated in a clear epoxy as shown in figure 4.4a. The transport coils are then mounted into a large brass plate that defines the coil positions in the experiment as well as provides cooling via low pressure water. T1-T13, MOT, and PUSH are all wound in this manner.

4.5 QUIC trap

Following magnetic transport from the MOT chamber, the atoms come to rest in a quadrupole trap labeled QUAD in figure 4.1. As mentioned before, a quadrupole trap by itself is not suitable for RF evaporation, so we smoothly ramp up the Ioffe

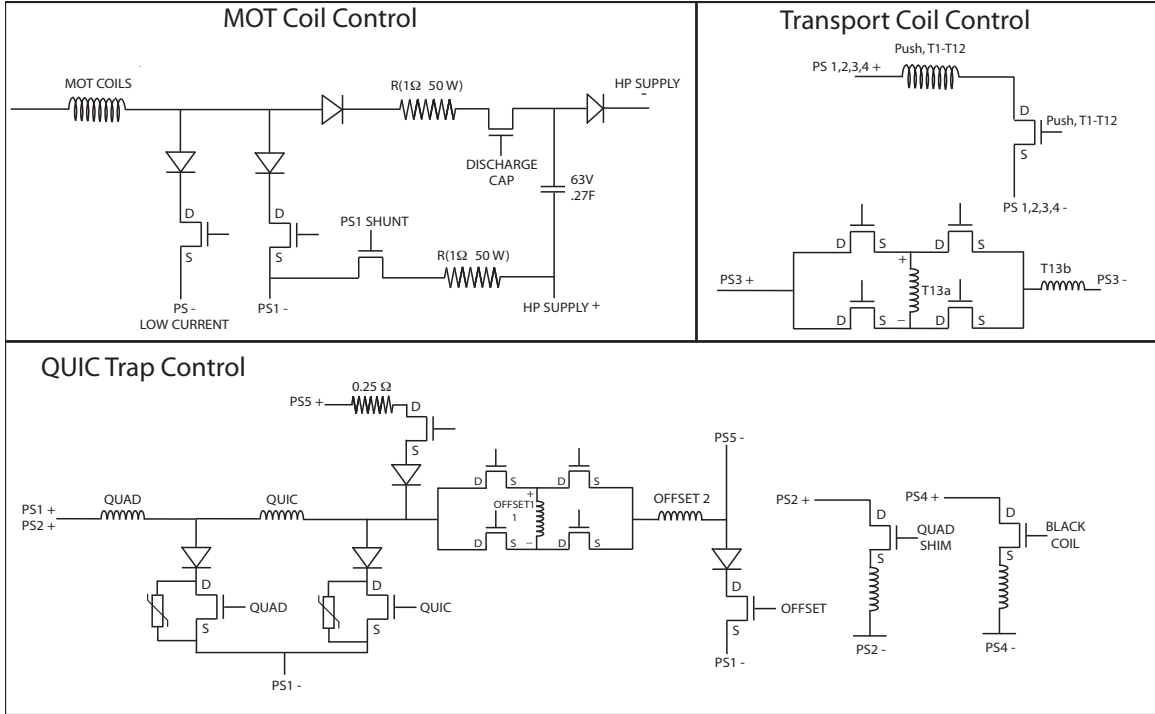


Figure 4.3: Schematic of circuits that control magnetic fields in the experiment. T1-T13 and PUSH are used to transport the atoms from the MOT chamber to the glass cell. QUAD, IOFFE, and OFFSET constitute the coils used to implement our QUIC trap. Quad shim, quic shim, T13, and black coil are used to control the position of the BEC in the spherical trap.

and offset coils in figure 4.1 to smoothly change the trap geometry from a quadrupole to a QUIC geometry. The QUIC trap is composed of a quadrupole pair, an Ioffe coil, and a set of offset coils. The topology is based upon the original design by Esslinger *et al.* [27].

4.5.1 QUIC topology

Typical setup

In the standard QUIC configuration, the current in the Ioffe coil is slowly ramped up while the current in the quadrupole coils is held constant. During the rampup of

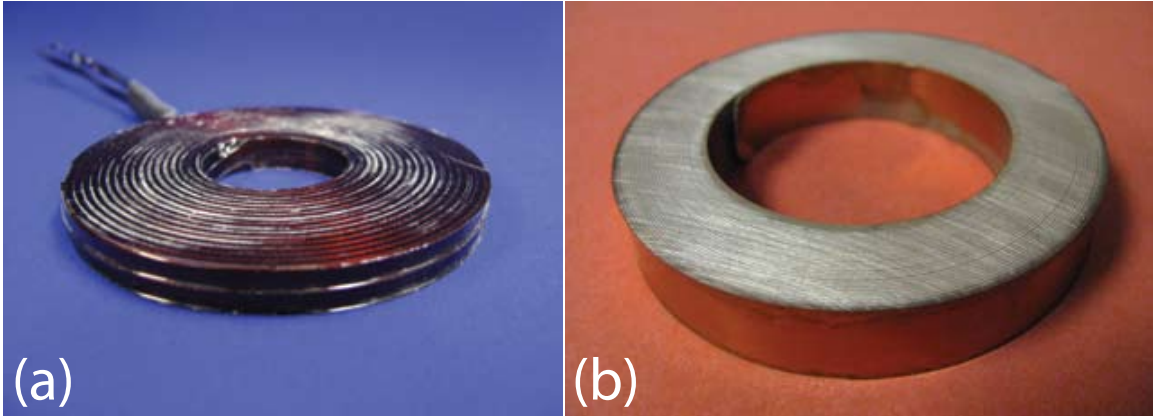


Figure 4.4: (a) Transport coil wound from insulated rectangular wire with a cross section of 1mm x 2.5mm. (b) Custom made spiral coil made from bare rectangular copper wire. The rectangular wire has a high aspect ratio of ≈ 30 . During the winding process we insulate it in the radial direction with a thin $50\mu\text{m}$ kapton layer, but the top and bottom sides remain exposed.

the Ioffe coil, the quadrupole trap center is shifted significantly towards the glass cell wall as the configuration changes from quadrupole to QUIC. The resulting trap is cigar shaped with tight confinement along the two radial dimensions and a relatively weak confinement along Ioffe coil axis(axial direction). To adjust the confinement to be equal on all axes, we ramp up an independent bias field, tuning the confinement in the radial directions to match that of the axial direction.

Our setup

Our configuration is unique in the following way. When changing the trapping geometry from quadrupole to QUIC, we ramp up currents in both the Ioffe and offset coils as opposed to simply ramping up the Ioffe coil alone. In our trapping geometry, this produces a cigar confinement, unlike typical setups where this would produce a spherical confinement. Our setup has the advantage that the quadrupole trap center

does not shift appreciably during the transformation of the trapping potential from quadrupole to QUIC, keeping the atoms far away from the glass cell wall at all times. To achieve a spherical confinement in our setup, we ramp down the current in the offset coils. This differs from other experiments where the current in the offset coils would have to be ramped up. In some sense it is a QUIC trap with reverse logic with respect to the offset coils. The spherical magnetic trap is the starting point for all of our experiments with BEC, and since the offset coils are not required for the spherical magnetic trap, they are free to be used for other purposes.

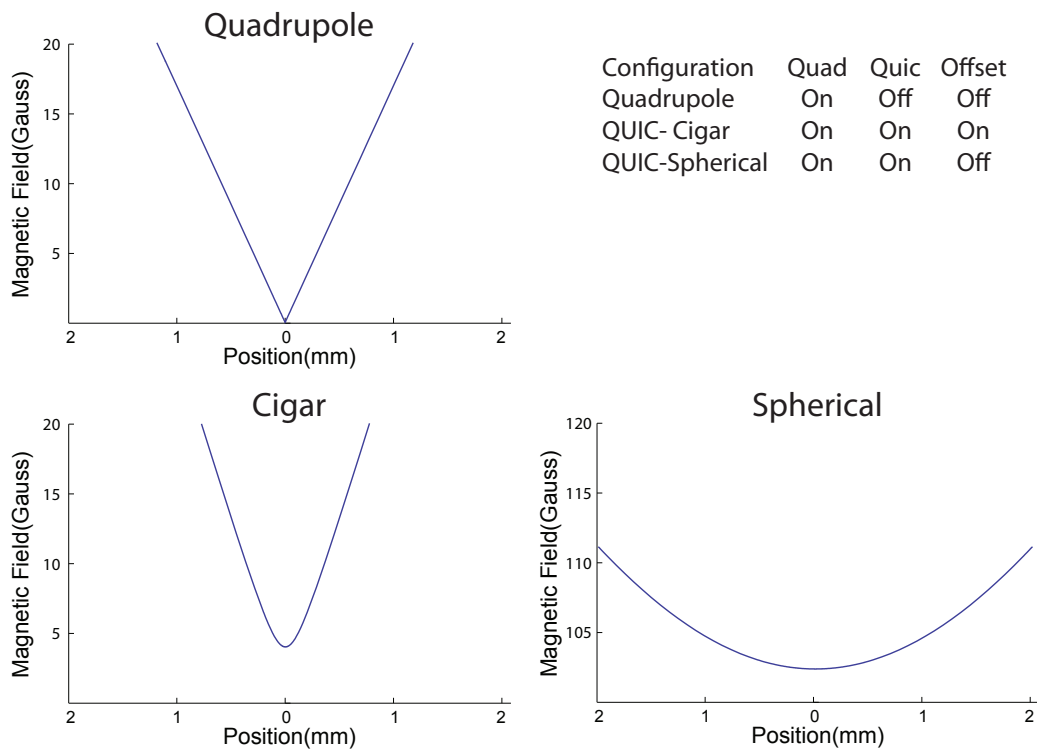


Figure 4.5: Magnetic trapping potentials for different configurations. With only QUAD energized, a quadrupole trapping potential is realized. With QUAD, QUIC, and OFFSET energized, a cigar type QUIC confinement is realized with an offset field of 4G. With QUAD and OFFSET, we realize a spherical QUIC trap with an offset field of 102G.

4.5.2 Physical design of QUIC trap

In previous experiments, coils for the QUIC trap were wound as shown in figure 4.4a. For this experiment, we implemented a new approach with the aim of maximizing thermal conductivity from the coil to the cooling source, allowing us to dissipate more power in the coils and at the same time allowing us to minimize thermal gradients in the air during the experimental cycle. In different approaches, the coils for the QUIC trap are insulated with a layer of kapton. The kapton provides crucial electrical isolation, but at the same time provides unwanted thermal isolation. We decided to go with an approach that removes the kapton insulation problem.

We use thin copper foil with a rectangular cross section to make our coils. We wind the copper foil together with a thin $50\mu\text{m}$ layer of kapton tape that insulates the windings from one another in the radial direction, but leaves the copper exposed on the top and bottom sides as shown in figure 4.4b. A low viscosity high temperature epoxy (EPO-TEK 301-2) is painted on the kapton tape during the winding process after which the coil is baked in an oven to heat cure the epoxy. The coil is then cut to the desired thickness. Initially, we tried to achieve this using an end mill, but the copper epoxy matrix was not suitable for this kind of machining. We found after some trial and error that a fly cutter was the best tool for the job. After fly cutting, the coils are sanded top and bottom with a fine grit sandpaper. It is important that the sanding be done on a very flat surface in order to avoid any non-uniformity in the flatness. Uniform flatness is verified by painting the coil with a black marker and making sure that the ink comes off uniformly after only a few "figure-eights" of sanding. After all preparations are complete, we scan each coil into the computer

and inspect for any short circuits due to small copper fragments bridging the tiny gap between adjacent windings.

We glue the coils to their respective heat sinks using a thermally conductive electrically insulating high-temperature epoxy (EPO-TEK 930-4). The particle size of the Boron-Nitride powder in the epoxy is specified as less than 20 μm allowing us to use a very thin layer to glue the coil in place. We control the thickness of this thin layer by mixing a small amount of glass beads ($r=25 \mu\text{m}$) into the epoxy that act as spacers, maintaining a constant thickness of epoxy between the coil and the heat sink. This unique procedure maximizes the thermal conductivity between the coil and heat sink. Our improved design enables us to move the QUIC trap closer to the center of the glass cell through the dissipation of more power in the Ioffe coil relative to the quadrupole pair, while at the same time ensuring that no part of the coil heats to more than 35 C during the experimental cycle.

4.6 Controlling the trap position in the spherical trap

The production of a BEC is only the beginning step of the experiment. In the next step we will be loading atoms into an evanescent wave surface trap, requiring that the atoms be positioned precisely in order to achieve successful loading. We control the atom position by using a combination of coils that are placed near the glass cell as pictured in figure 4.8. The bias coil configuration is changed from Helmholtz to anti-Helmholtz in order to shift the atom position along the Ioffe coil axis. The quad



Figure 4.6: (a) Jig used to wind the bias and quad coils. (b) a teflon sleeve is wrapped around the center part of the jig and a slit is cut to facilitate the beginning of the winding process. (c) Jig used to wind the Ioffe coil. (d) Same as (b) except smaller because it is for the Ioffe coil. (e) The winding process consists of winding a copper tape and Kapton tape together tightly around the jig. Close inspection of the picture reveals a brush in one of the gloved hands, applying a low viscosity epoxy throughout the winding procedure. Immediately following the winding process, cable ties are wrapped around the coil to keep it tight while it is baked to cure the high temperature epoxy. (f) After the coils are wound and the epoxy fully cured, we fly cut the coils to the desired thickness. (g) A zoomed-in picture taken through a microscope showing the uniform spacing of the copper layers and lack of defects.

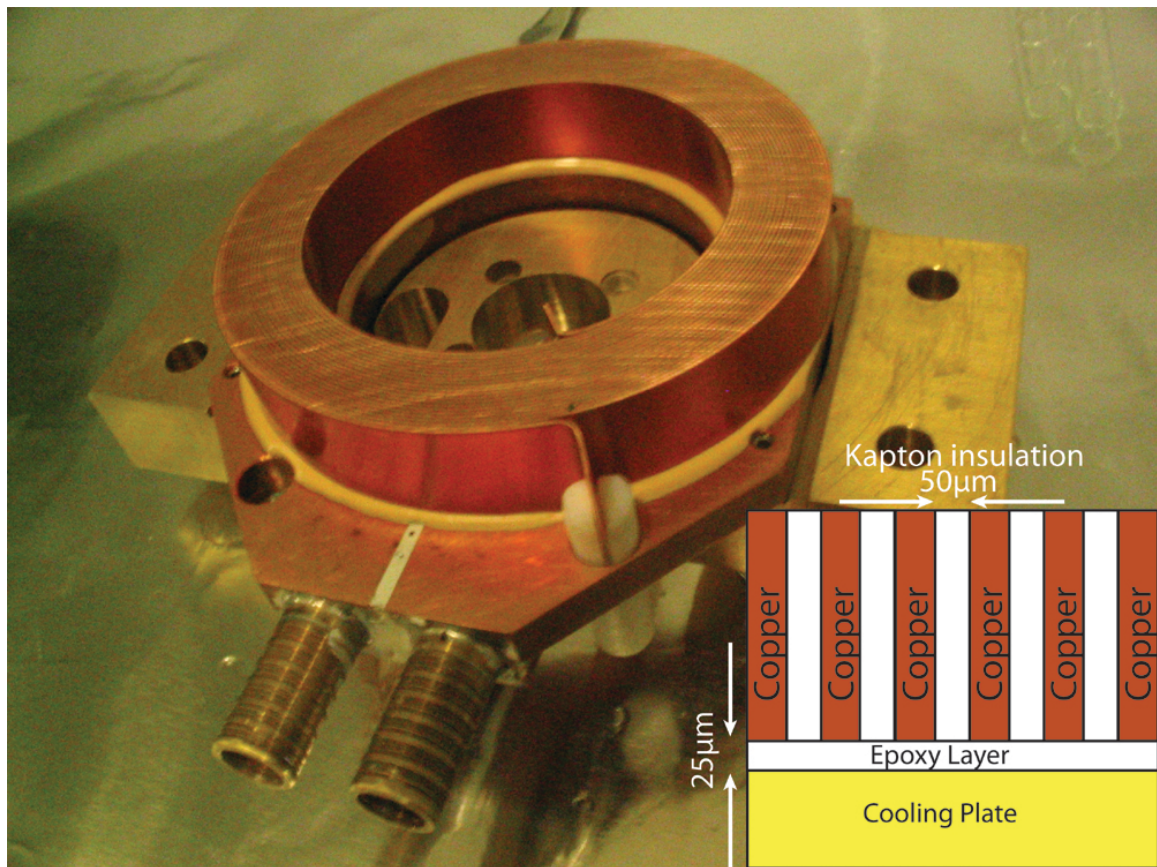


Figure 4.7: New coil design. The copper coil is mounted with thermally conductive epoxy to the heat sink. The heat sink is custom-designed to allow maximum optical access to the atoms while providing mechanical support to the coil. The heat sink consists of two copper pieces that have cooling channels milled into them before they are soldered together. This design allows us to use low pressure water to carry away the heat generated during the experimental cycle.

shim coils are in a Helmholtz configuration that shifts the atoms along the quadrupole axis and the black coil acts together with the last transport coil (T13) in order to control the position of the atoms along the remaining axis.

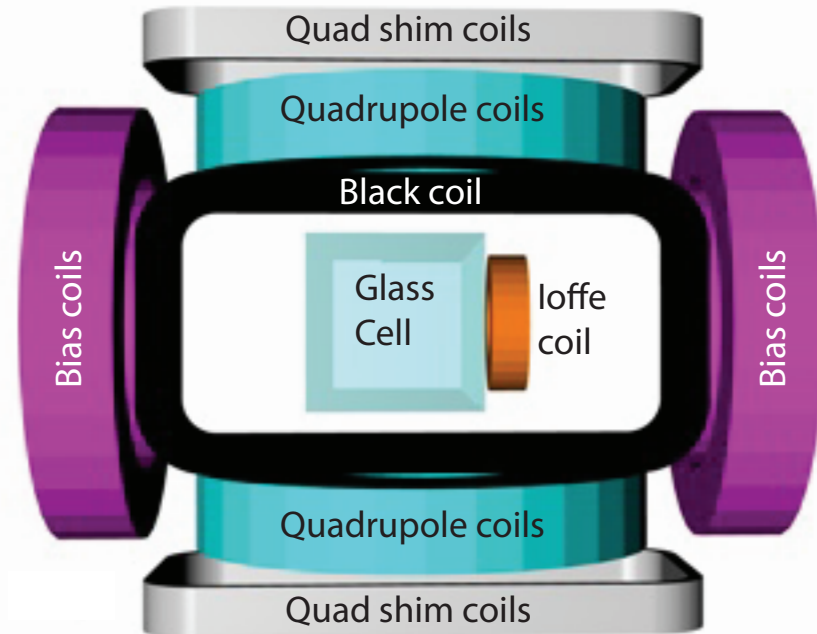


Figure 4.8: Coils surrounding the glass cell where the BEC is created. The quadrupole coils together with the Ioffe coil form a spherical magnetic trap. The center of the spherical magnetic trap can be adjusted in all three dimensions by using the quad shim coils, bias coils, and the black coil. Three-dimensional control is necessary to position the atoms directly below the center of the hemisphere (not pictured).

Chapter 5

Evanescent wave surface trap

5.1 Introduction

Evanescent waves were first introduced to atomic physics in the context of creating mirrors [6, 55] for atom optics. Later, evanescent waves found use in a novel surface trap for cold atoms [65, 41] where a two dimensional Bose-Einstein condensate (BEC) was created [75]. Evanescent waves have proven to be a useful tool in atomic physics when there arises a need to work with atoms near a surface. Since we require our atomic ensembles to be within a few microns of a surface in order to realize a high resolution solid immersion microscope for cold atoms, an evanescent wave surface trap is natural choice for our experiment. The short length scales of evanescent waves allow for high trapping frequencies which is an added bonus for our experiment because the high trapping frequencies allow us to enter the 2D regime with our quantum gas. However, previous experiments have found evanescent waves to be susceptible to stray light scattered by impurities on surfaces [55, 75]. In our setup we explore new methods

of alleviating the problem of stray light by working not only with a superpolished ultra clean surface, but also employing broadband light [18] to mitigate the effects of any remaining stray light in the system.

5.2 Evanescent waves

A beam of light traveling from a high index of refraction material to a low index material will undergo total internal reflection for angles of incidence greater than the critical angle $\theta_c = \arcsin n_2/n_1$. For angles greater than θ_c there is an exponentially decaying light field penetrating into the low index material, this is what we call an evanescent wave(EW). The intensity of the EW penetrating into the low index material is given by the functional form $I_0 e^{-\frac{2z}{\Lambda}}$ where I_0 is the intensity of light at the interface where the reflection occurs [39] and the decay length Λ is given by $\Lambda = \lambda/2\pi(n^2 \sin^2(\theta) - 1)^{-1/2}$.

Evanescent waves are very useful when working with atoms near a surface because they offer a way to overcome the van der Waals potential which is attractive and very strong close to the surface. Using a blue detuned laser beam ($\delta > 0$) to form an evanescent wave creates a repulsive potential for the atoms given by equation 2.10 where the intensity has a Gaussian profile in the lateral dimensions and decays exponentially in the direction normal to the glass-vacuum interface.

We create an evanescent wave by sending a laser beam through one of the entrance facets of the hemisphere as shown in figure 5.1a. The laser beam is then totally internally reflected at the glass-vacuum interface, creating an evanescent wave potential penetrating into the vacuum region. To compensate for the large angle of incidence

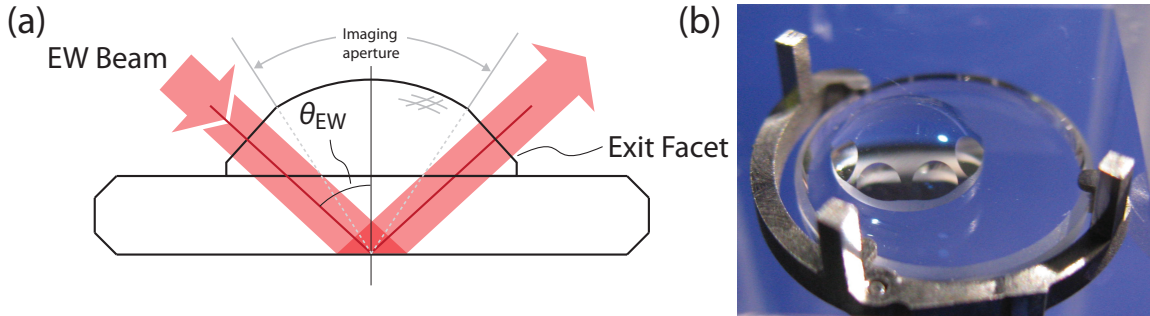


Figure 5.1: (a) Schematic of hemisphere, formed by optically contacting a high quality superpolished substrate with a beveled partial hemisphere. (b) Picture of hemisphere mounted in vacuum chamber.

of the laser beam, we shape the beam to be elliptical, which allows us to achieve a circular potential for the atoms in the lateral dimensions. We control the angle of incidence of the EW beam by using a combination of optics and a motorized mirror mount that allows us to change the angle of the EW beam independent of the EW beam position in the plane of the atoms. To align the angle of the EW beam, we scan the motorized mirror mount and record the transmitted light power on a photodiode. Examining the data, we can perform a fit to find the critical angle as a function of motor position. This allows us to precisely control the decay length of the evanescent wave by setting the motor position accordingly. It is crucial to set the motor position correctly, otherwise it is possible to have a traveling wave component mixed in with the EW. The traveling wave component will exert transverse forces that depend upon the vertical position of the atoms cloud, complicating the loading procedure immensely.

5.3 Susceptibility of evanescent waves to surface scatter and uncontrolled interferences

Uncontrolled interferences in the experiment can lead to serious distortions of the intended optical potential. In this experiment we make use of both standing waves and evanescent waves, with their susceptibility to scattered light being very different. Scattered light from a standing wave interfering coherently with the original standing wave causes intensity modulations given by $I_{modulation} \sim \sqrt{I_{trap}I_{scattered}}$. Thus, scattered light even at the 10^{-6} level will cause modulations at the 10^{-3} level. The EW is inherently more susceptible to stray light interferences than a standing wave for the following reason. At the superpolished surface where the majority of scattering occurs, the EW is maximally intense, while at the position of the atoms the EW is only a small fraction of its initial intensity since the atoms are held a few EW decay lengths away from the surface of the superpolished substrate. This means that even a small scattered fraction from the surface can potentially overwhelm the EW at the position of the atoms. It is for this reason that we take extraordinary steps to reduce the effects of scattered light in this setup.

5.3.1 Broadband light

As our first defense against unwanted modulations in the EW trapping potential, we disable the interference between the trap light and most of the stray light from reflections, dust and surface imperfections by using “white” light with a very short coherence length. The light is created by a two-stage tapered amplifier (TA) system,

delivering 400 mW of light. The TAs are seeded with 6 mW of light from a fiber coupled amplified spontaneous emission (ASE) source. Interference filters before and after the TAs are used to control the bandwidth of the white light source as well as to suppress resonant ASE components. The resulting approximately 3 nm wide spectrum is centered around a wavelength of $\lambda_{trap} = 765$ nm, with an incident power of 200 mW. We measure a coherence length of $160 \pm 10 \mu\text{m}$ (50% decay path length difference), which is short enough to suppress the interference effects of stray light from multiple reflections in the glass substrate as well as most scatterers outside the radius given by the coherence length.

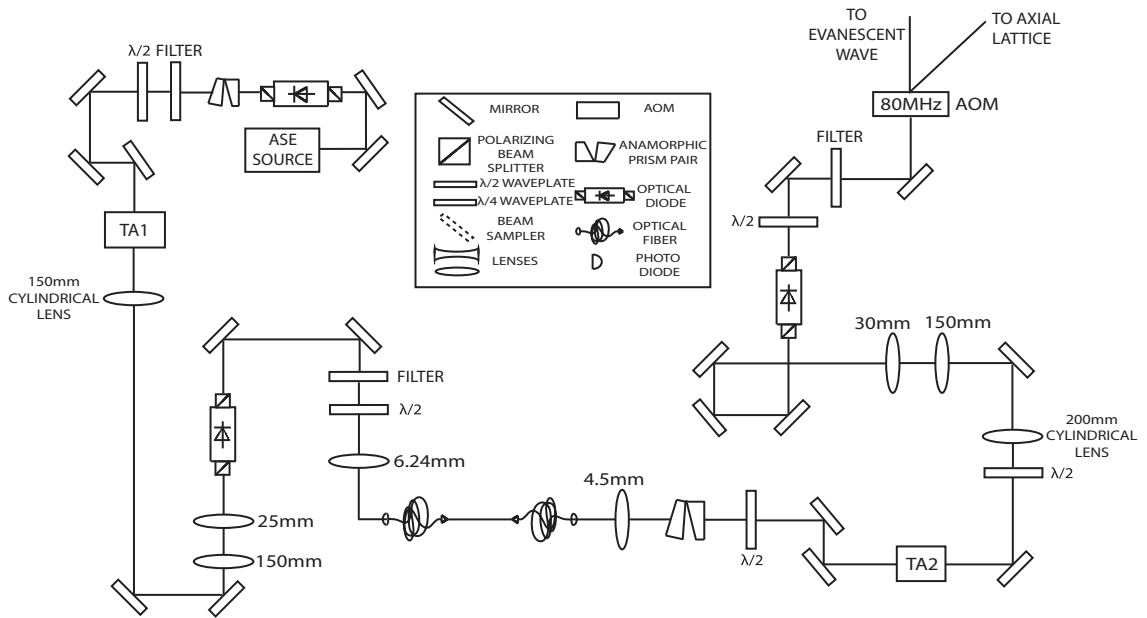


Figure 5.2: Laser setup for the generation of a high power broadband light source.

5.3.2 Superpolished substrate

A second measure employed for reducing inhomogeneities in the optical trapping potential is the minimization of scatter at the trapping surface by using a superpolished and very clean surface with an RMS surface roughness below 1 Å. We measured the scattering properties of the superpolished surface as follows. Our setup consists of a high numerical aperture microscope objective focused in the plane of the superpolished surface and a green laser beam at a grazing incidence to the superpolished surface such that none of the green laser beam travels into the microscope objective. We then use a CCD camera to measure the total light collected by the objective, thereby measuring a fraction of the total light scattered from the surface. We then normalize this number to the amount of light scattered by a piece of paper placed in the same plane, assuming that the paper is a perfect scatterer. We find that the superpolished surface scatters light at the level of 10^{-7} . By changing the focal plane of the microscope objective we can also measure the scattering from the unpolished side as well and we find that it scatters at the level of 10^{-5} , so the superpolishing process wins us a factor of one hundred.

5.3.3 Adsorbates on superpolished surface

Neutral atoms in close vicinity to surfaces can also be affected by static electric potentials. Adsorbed metal atoms on the surface form small electric dipoles. Inhomogeneities of the distribution of these dipoles generate potential gradients which can be stronger than the inherent van der Waals force of the substrate. This process is well understood [58, 63] and the fields generated decay very rapidly away from the surface.

By minimizing rubidium deposition on the glass, detrimental effects are avoided at a moderate distance of $1.5 \mu\text{m}$ from the surface.

5.3.4 General lab cleanliness

The optical contacting [73] of the superpolished substrate to form the hemisphere is done under an enclosed HEPA filter, keeping the custom optic free of dust and contamination. All of this is wasted though if the optic is contaminated upon being removed from the protected HEPA environment and inserted into the vacuum chamber. To avoid any contamination during the transport and insertion process, we created a clean room environment around the entire vacuum chamber. All horizontal surfaces were wiped clean of dust and all non-essential objects were removed from the area. Clean room suits were required to enter or work in the area in order to maintain a low dust environment. All of these precautions allowed us to keep the superpolished surface clean and free of dust while mounting it inside of the vacuum chamber.

5.3.5 Mechanical mounting of the hemisphere

We mount the hemisphere inside of the vacuum chamber with a clamp and a set of rods that are connected as shown in figure 5.3. A stainless steel clamp (5.3a) with three extrusions protruding upwards holds the hemisphere in place while at the same time defining the position of the hemisphere with respect to the glass cell. A long thin rod is press fit into the clamp on one end and is connected via set screws to the interconnect piece on the other end. The interconnect piece (5.3b) slides freely

into the thick rod with a spring in between to allow the application of a defined force to the assembly above and including the interconnect piece. A thick rod below the interconnect threads directly into a conflat flange (5.3c) and is held in place with a locking nut. The conflat flange is shown in more detail in (5.3d). In addition to providing mechanical support to the hemisphere mounting assembly, a large hole is cut into the flange creating optical access from below the chamber that allows us to perform absorption imaging. The conflat flange is attached to an xy tilt stage that allows us to position the hemisphere in the xy plane and the tilt stage is attached to a stainless steel bellows with attached z-stage that allows us to control the z position of the hemisphere. Using these degrees of freedom, we are able to precisely position the hemisphere in three dimensions.

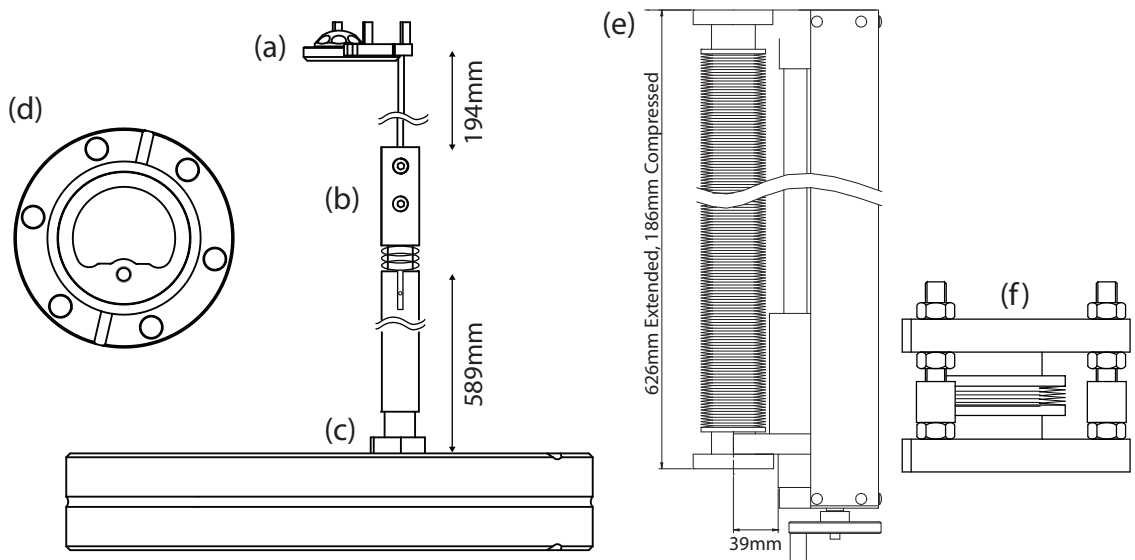


Figure 5.3: Mechanical setup for mounting of hemisphere. Assembly is attached to an xy tilt stage combined with a linear translation stage along z.

5.4 Loading the evanescent wave surface trap

The evanescent wave trap configuration is formed by moving the spherical magnetic trap vertically upwards using external magnetic fields generated by the last transport coil pair T13 and the black coil, see fig.4.8. We use quad shim and quic shim respectively (fig.4.8) to control the atom position in the x-y plane. The atoms are positioned directly below the evanescent wave potential, then the magnetic trap center position is moved by 1.6 mm in the z direction, well beyond the glass vacuum interface. When the magnetic trap center moves beyond the surface, the atoms are vertically held in place by the EW, giving rise to a combined opto-magnetic surface trap (Fig. 5.4d). In the combined opto-magnetic surface trap, the vertical confinement is given by the combined evanescent wave and magnetic potentials and the lateral confinement is provided by the magnetic trap which dominates over the weak anti-confinement due to the evanescent wave potential. While we take great care to move the magnetic trap center as slowly as possible during the loading of the EW trap, the length scale of the EW is sufficiently short and the trapping frequency in the spherical magnetic trap is sufficiently small such that the loading is inherently non-adiabatic to some degree. The non-adiabatic nature of the loading process leads to heating of the sample by a few tens of nanokelvin.

The EW beam is an elliptic beam of $250\ \mu\text{m} \times 180\ \mu\text{m}$ size incident at an angle θ_{EW} , 12 mrad from the critical angle θ_c (Fig. 5.4a) corresponding to a decay length of $\Lambda \approx 800\text{nm}$. The overall potential is repulsive up to a maximum at a distance of $\approx 200\text{nm}$ from the surface, below which the attractive van der Waals potential dominates (Fig. 5.4b). The short decay length of the EW gives rise to large curvatures

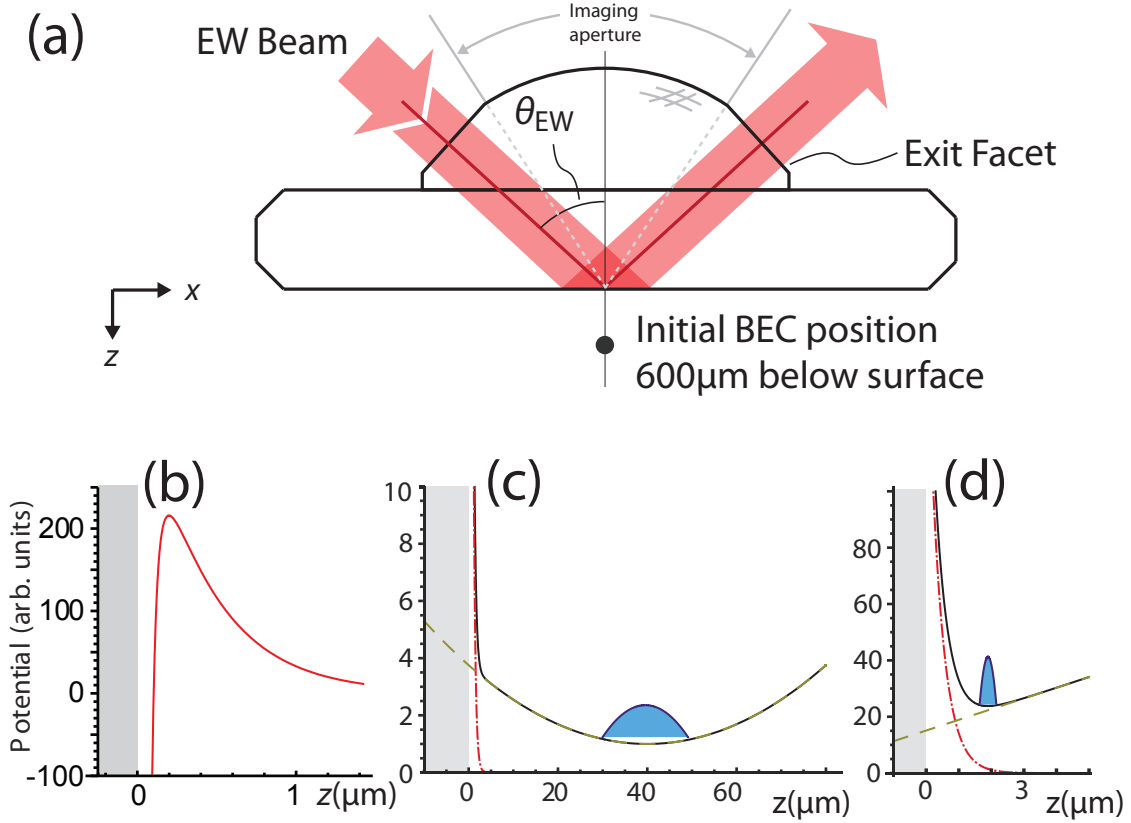


Figure 5.4: (a) Setup for creating evanescent wave(EW) surface trap. (b) Combined evanescent wave and van der Waals potential. (c) BEC in spherical magnetic trap. (d) Atoms loaded into EW surface trap.

that allow tight confinement along the direction of the decay.

5.5 Analysis and results

Loading an evanescent wave surface trap is not a trivial exercise as the atoms need to be aligned to the EW beam before there is any signal to optimize. Needless to say, we were all very excited when we loaded the surface trap for the first time and could then begin to test its performance. One of the first things we checked was the EW confinement by measuring the trap frequency. We did this by adding a small

modulation to the EW potential and then scanning the modulation frequency. As we vary the modulation frequency of the EW, we expect to see an atom loss that is peaked at the trapping frequency. The results of the trapping frequency measurement are plotted in figure 5.5 showing a trapping frequency of close to 775Hz. We are able to push the trapping frequency up to 1kHz in the EW configuration, allowing us to reach the 2D regime with $\hbar\omega \gg \mu_{3D}$. It is worth noting that the trapping frequency in the vertical direction can also be found by examining the vertical extension of the cloud in a time of flight measurement; we perform this measurement as well and find it to be in good agreement with the parametric heating results.

The use of broadband light for the generation of the EW potential is designed to reduce the effects of stray light in the system. However, the use of broadband light also introduces the possibility of unwanted trap loss due to processes such as photoassociation. It is for this reason that we were very eager to measure the lifetime of the atoms in the EW trap. Our fears of excessive atom loss were unfounded as we measured a $1/e$ atom lifetime in the EW trap of $\tau = 17 \pm 1$ s (Fig. 5.5b) that is limited by background gas collisions.

It is of paramount importance that we obtain a low temperature sample in the 2D EW configuration to ensure that the quantum gas is below the BKT transition temperature T_{BKT} . After loading the atoms into the EW trap, we experimented with a forced evaporation whereby we lowered the power in the EW beam such that the potential barrier height to the surface was gradually lowered, allowing the hottest atoms to tunnel to the surface, leaving behind a colder and denser sample. Unfortunately, this method proved to be problematic in the following sense. The atoms that

evaporated to the surface created localized patches of adsorbed surface dipoles which lowered the potential barrier and eventually rendered the location unusable until the adsorbates redistributed over the surface. Due to this effect of the adsorbates, we did not pursue this method further and rather pursued a forced evaporation in the axial lattice trap which is discussed in the next chapter.

The main motivation for using a superpolished substrate and broadband light was to obtain a maximally homogeneous EW lateral potential such that we could avoid the pitfalls of previous experiments that utilized evanescent waves. To verify the lateral homogeneity of the resulting potential, we dynamically transported the cloud over the diameter of the EW beam (by displacing the magnetic field center up to $250\ \mu\text{m}$) without causing significant heating or atom loss due to “holes” in the evanescent wave.

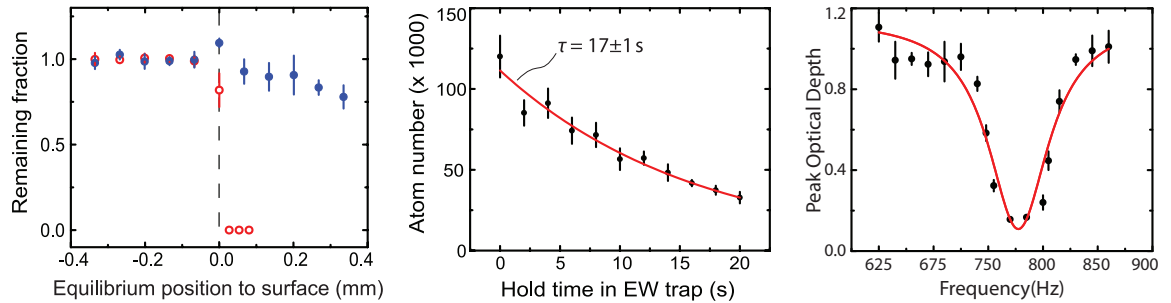


Figure 5.5: (a) Remaining fraction of atoms as a function of distance from glass surface. Hollow red circles show that when the evanescent wave is off, the atoms are lost when the quantum gas reaches the surface. Solid blue circles show that this is not the case when the evanescent wave is on. (b) Lifetime of atoms in evanescent wave surface trap. (c) Measurement of trap frequency via parametric heating.

5.6 Summary and outlook

We demonstrate a successful evanescent wave surface trap with a 2D pancake like confinement. The atoms in the EW surface trap sit only a few μm away from a fused silica surface, allowing us to exploit a solid immersion effect that will allow for high resolution imaging in later steps of the experiment. Implementing a novel approach using broadband light we minimize the effects of stray light in the system, we are able to realize a smooth EW potential with long trapping lifetimes. However, the EW surface trap is not the end of the story as we will now load the "pancake" into a single well of a one dimensional standing wave in order to further insulate the atoms from the effects of any remaining disorder due to stray light in the system.

Chapter 6

1D axial lattice

6.1 Introduction

The evanescent wave (EW) surface trap allows us to enter the 2D regime with our quantum gas in a controlled and reproducible way. However, for future experiments we require optical potentials with minimal disorder for the observation of many-body states. To this end, we transfer the atoms from the evanescent wave surface trap directly into a single minima of a one dimensional standing wave. The standing wave (SW) trap enjoys multiple advantages over the evanescent wave trap. The SW trap offers improved protection against unwanted scatter from impurities on the superpolished surface. In contrast to the EW which has an intensity maximum at the superpolished surface, the SW has an intensity node which minimizes the amount of scattered light from the impurities on the surface. In this way, we realize a maximally smooth potential for the atoms. Additionally, the SW trap provides a tighter confinement in the vertical direction, allowing us to create condensates deep in

the two dimensional regime even for large atom numbers. The increased confinement in the vertical direction also increases the on-site interaction in the system, allowing us easier access to many-body states such as the Mott insulator.

6.2 Comparison of evanescent wave trap to standing wave trap

The SW offers significant improvement over the EW in terms of creating an efficient confinement for the atoms. For a given trapping frequency of $\sqrt{4g/\Lambda}$ and assuming a distance of 2Λ from the surface, the potential depth U_{ew} of the EW is roughly $\Lambda mg \cdot e^4$ while for the SW the potential depth U_{sw} is given by $mg\lambda^2/(2\pi^2\Lambda)$. Approximating $\lambda \sim \Lambda$, the ratio of potential depths is $U_{ew}/U_{sw} \sim 1000$, meaning that for a given trapping frequency the SW trap requires only one thousandth the intensity of its EW counterpart.

The SW also offers a significant advantage over the EW in terms of light levels at the surface of the hemisphere. The EW potential is maximal at the surface leading to a maximum amount of scattered light. In contrast, the SW potential has an intensity minimum at the surface that is a small fraction of the incoming intensity. The fraction of light at the surface is $1+r^2-2r \sim .14$ where r is reflection coefficient for the incident electric field [42].

In our setup we use the SW to increase the vertical trap frequency by a factor of ten while still using ten times less light intensity than the EW. Once the suppression of scatter is taken into account at the surface of the glass, the SW has not only

increased the vertical confinement but additionally the scattered light at the surface is suppressed by a factor of ~ 100 .

6.3 Axial lattice surface trap

The standing wave potential is generated by reflecting a blue-detuned beam off the glass surface [26] from the vacuum side as seen in figure 6.1a. Incident at an angle $\theta_{SW} = 75^\circ$ from the normal, the trap minima in the resulting potential are planes parallel to the surface with a spacing of $\approx 1.5\mu\text{m}$. Compared to the evanescent wave configuration the trapping frequency is increased by a factor of more than 5. Contrary to all current standing wave traps [80, 52, 79], the potential is formed not by coherent light but by light from the 765 nm broadband source. This reduces disorder from stray light interference, but does not significantly affect the interference contrast, as the coherence length of the light is still much larger than the interfering distance $2d \cdot \cos \theta_{SW}$. The SW configuration also reduces further the disorder caused by remaining scattered light interference from those parts of the glass which are closer than the coherence length. As the SW has an intensity minimum at the surface as opposed to the intensity maximum of the EW, scattering from small surface impurities is suppressed.

6.4 Setup

We reliably load all of the atoms into a single node of the standing wave, as the spread of the wave function ($z_{ho} = 250\text{ nm}$) in the pure EW trap is much smaller than

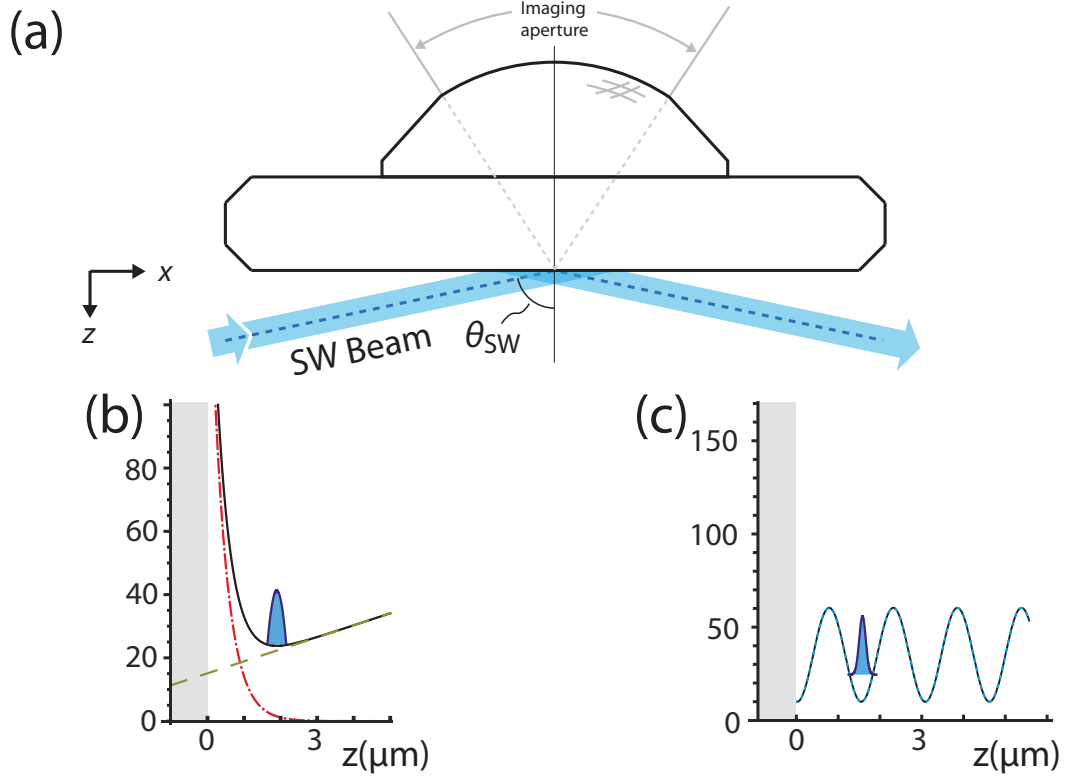


Figure 6.1: (a) Setup for creating 1D standing wave surface trap. (b) Atoms in combined evanescent wave and magnetic potential. (c) Atoms loaded into 1D standing wave trap.

the spacing of the SW planes. The transfer is realized by smoothly shifting power from the EW beam to the standing wave beam over a period of 300 ms. The trap frequency in the z direction, verified by parametric excitation measurements, is increased to 5.9 ± 0.1 kHz in this trap, taking us deep into the 2D regime with the temperature and chemical potential both much smaller than the vertical trap frequency. We populate the first node of the SW at a distance of $\approx 1.5 \mu\text{m}$ from the surface. In this plane, the disorder caused by surface dipoles is already strongly reduced, but the distance from the surface is small enough to exploit the NA enhancement when imaging through

the substrate. In order to confirm the lateral homogeneity of the potential, we move a bimodal ensemble $200\ \mu\text{m}$ back and forth across the surface within 150 ms. We do not observe any heating ($\Delta T = -4.3\text{nK} \pm 4.0\text{nK}$) or atom loss ($\Delta N/N = 3.4\% \pm 2.4\%$) during this process. Another indication for the smoothness of the potential is that the atoms are free to leave it by moving out of the beam within a few 10 ms when switching off the magnetic potential, due to a weak remaining anti-confinement. The $1/e$ lifetime in the SW trap is $7.8 \pm 0.4\text{s}$, and we have used both the incoherent light and a narrow band 765 nm CW Ti:Sapphire laser for comparison. We find the lifetimes to be the same within the error of the measurements and consistent with loss due to spontaneous emission, indicating that there are no additional loss/heating processes (e.g. photoassociation) associated with using the broadband light source.

6.5 Characterization of quantum gas in the 2D regime

The 2D regime manifests itself as a change in the shape of the momentum distribution measured in time of flight along the z direction. We obtain a Gaussian momentum profile along the vertical (Fig. 6.2a) corresponding to the harmonic confinement of the trap, while the profile along the other direction remains Thomas-Fermi (Fig. 6.2b). The 2D system with $\approx 2 \times 10^4$ atoms is below the expected BKT transition temperature of $T_{BKT} \approx 40\text{ nK}$ at which vortices proliferate in the condensate [11]. Below T_{BKT} , phase fluctuations in the condensate fraction can be present which are mapped to density fluctuations [24] in time of flight as seen in Fig. 6.2c. These fluctu-

ations decrease with the temperature of the condensate during a second evaporation step.

6.6 RF evaporation in the standing wave

The SW configuration allows us to perform forced RF evaporation inside the 2D trap using a radial magnetic field gradient to evaporate along the outer edge of the trap volume. By stabilizing the current for the bias magnetic field of the QUIC trap to ~ 3 ppm, we obtain a stable evaporation process with reproducible atom numbers in the desired range of several 10^4 atoms. The RF evaporation provides a way to control the temperature of the ensemble in the 2D trap, allowing us to move well below T_{BKT} in order to realize a condensate with minimal phase fluctuations.

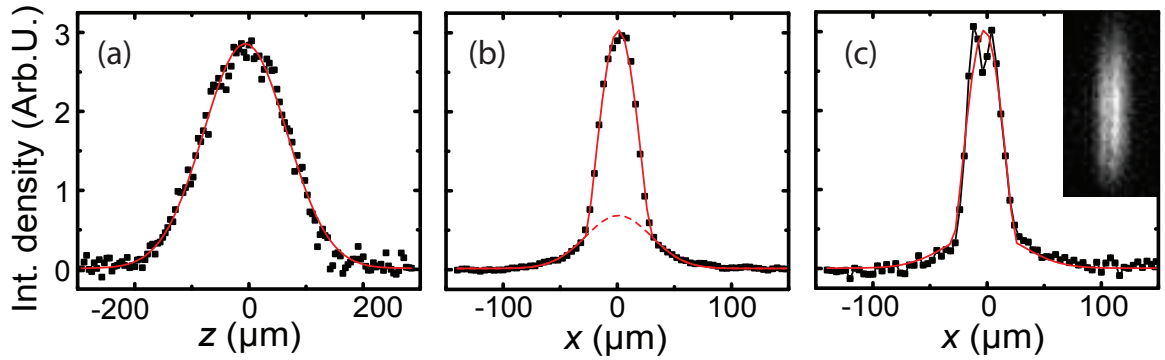


Figure 6.2: Quantum gas deep in 2D regime. Time of flight images from standing wave trap: (a) the vertical density profile is Gaussian, showing that the system is deep in the 2D configuration. (In the lateral direction, it is well described by a bimodal Thomas-Fermi profile with $\approx 20\%$ thermal fraction in this case), (b) integrated lateral profile averaged over 86 samples, (c) density fluctuations caused by thermal 2D phase fluctuations in single profile from same data set (inset shows $140 \mu\text{m} \times 280 \mu\text{m}$).

6.7 RF spectroscopy in the 1D lattice

We can also intentionally load two planes (here the first and second) of the SW trap by weakening the confinement and choosing a larger separation from the surface in the initial EW configuration. When two planes are loaded, a vertical sinusoidal interference pattern appears after ballistic time of flight (Fig. 6.3), which can be used to detect long-range phase fluctuations and vortices in the trap [80]. In order to quantitatively probe the distribution over the trap nodes, we employ RF spectroscopy similar to that done in [80], using a magnetic field gradient of 33.8 ± 0.7 G/cm perpendicular to the surface. The density distribution along the gradient direction is then probed by varying the RF frequency according to a scaling of 2.43 ± 0.05 kHz/ μm . This achieves a spatial resolution better than $1 \mu\text{m}$. The vertical potential periodicity is $1.54 \pm 0.04 \mu\text{m}$, determined by diffracting atoms off the SW. The profile is shown in Fig. 6.3d using an RF pulse length of 2s. The two loaded sites can be clearly distinguished. Conversely, when loading a single site, the profiling yields an upper limit for the occupation in the second site of $\approx 5\%$, while the (lack of) interference during ballistic expansion limits the fraction of the total coherent population in that site to less than $\approx 10^{-3}$. Loading two planes of the 1D lattice also gives us a way to observe thermally activated vortices via the interference pattern observed in time of flight images. In this way we can verify that temperatures reached during RF evaporation in the 2D trap are low enough to remove any thermally activated vortices from the system.

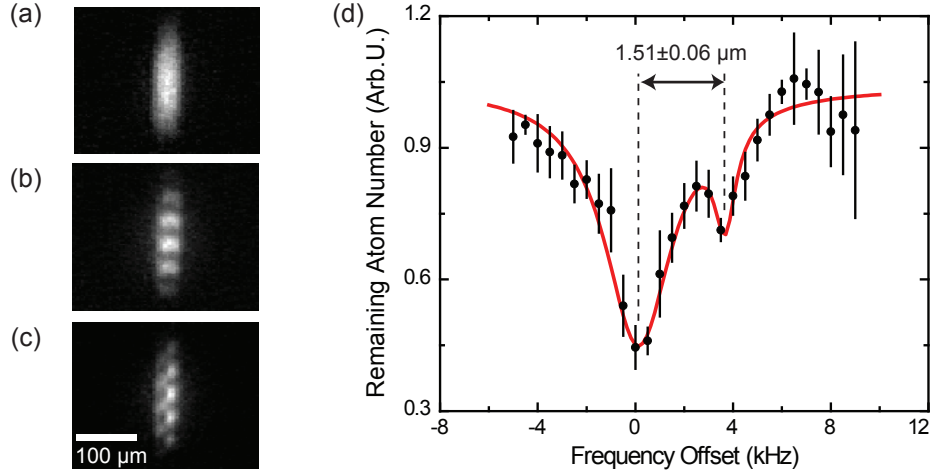


Figure 6.3: Loading of single and multiple planes in the standing wave trap. (a) atoms loaded into a single site, imaged from the side after release and 17 ms time-of-flight, (b) interference between atoms from two planes. (c) interference pattern between two planes at a higher temperature showing the presence of a thermally activated vortex. (d) The vertical density profile obtained by RF addressing shows the occupation of two planes. The red line denotes a two-peak Lorentzian fit, which yields a peak separation of $1.51 \pm 0.06 \mu\text{m}$.

6.8 Summary

In summary, we demonstrate a novel scheme of creating a quantum gas deep in the 2D regime close to a glass surface. The trap provides both strong confinement in the vertical direction and smooth potentials in the 2D plane without the necessity to load many planes simultaneously. We avoid interference of scattered light with the trap light by employing light sources which have short coherence lengths. We create 2D quantum gases and are able to detect properties such as phase fluctuations and thermal excitation of vortices. Through a second RF evaporation in the 2D trap we are able to control the temperature to be below T_{BKT} ensuring that our condensate has a uniform phase. We now look towards our broader goal of creating a system

for the study of many-body physics. In the next phase of the experiment we will take advantage of our high resolution imaging system which allows us to both project lattice potentials onto the atoms and detect single atoms on single lattice sites via fluorescent imaging.

Chapter 7

2D Lattice and imaging

7.1 Introduction

Having achieved 2D confinement of our quantum gas, we are now in position to make use of our high numerical aperture (NA=.8) imaging system for not only high resolution imaging but also for the projection of lattice potentials. In contrast with previous experiments, our high numerical aperture optics enable the direct projection of optical lattices with lattice constants that are small enough to allow for the study of many body physics. After the atoms have been successfully loaded into the 2D lattice, we then image the entire 2D lattice via fluorescence imaging. Employing an optical molasses during the imaging process that allows us to "freeze" the density distribution of the atoms in the lattice, we are able to detect single atoms with high fidelity.

7.2 Imaging system

The imaging system consists of a long working distance (18mm) microscope objective that sits outside of the vacuum chamber, together with a hemispheric lens that sits inside of the vacuum chamber as shown in figure 7.2a. The objective is diffraction limited with a numerical aperture of $NA=0.55$. Since our quantum gas sits only a few microns away from the surface of the hemisphere, the hemisphere inside the chamber gives rise to a solid immersion effect that allows us to increase the numerical aperture of the imaging system by the index of refraction of the hemisphere ($n=1.45$). The numerical aperture of the combined imaging system is $NA=0.8$, corresponding to a diffraction limited resolution of $\approx 500\text{nm}$. The microscope objective is aligned interferometrically to the hemisphere (figure 7.1).

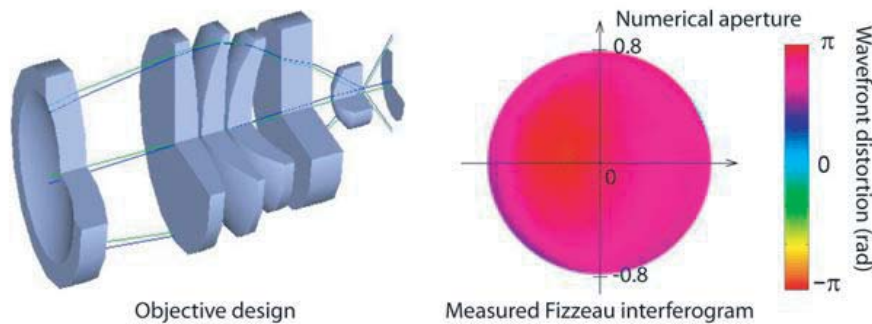


Figure 7.1: Three dimensional image of the imaging system and measured interferogram showing a diffraction limited performance.

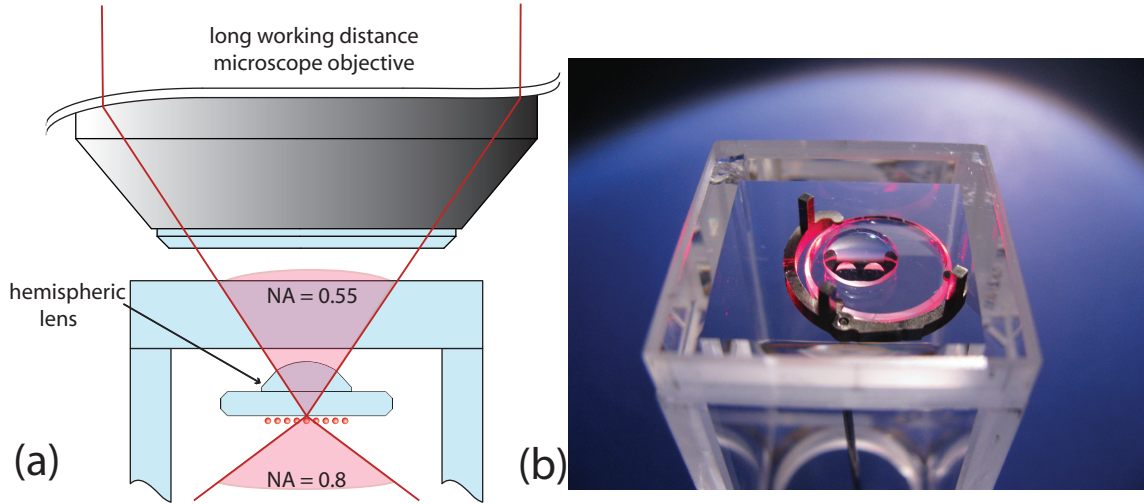


Figure 7.2: Imaging System: (a) Schematic of the imaging system, composed of a long working distance microscope objective together with a hemispherical front lens. The hemispherical lens increases the numerical aperture of the system from $NA=0.55$ to $NA=0.8$. (b) Hemisphere mounted inside of glass cell, held in place by stainless steel clamp.

7.3 Mounting of the microscope objective

Due to the high numerical aperture of our imaging system, it is imperative that the imaging system does not shake with respect to the atoms. Since the atom position is defined by the hemisphere which is mechanically defined by the glass cell, we require that the microscope objective be mechanically attached to the glass cell to ensure that all vibrations are common mode. We mount the microscope objective to the glass cell via a stainless steel clamp (figure 7.3a) attached to the glass cell that acts as a mounting platform for a hollow tube of G10 (figure 7.3b) that is machined to allow passage of laser beams into and out of the glass cell. We then attach the microscope objective to a slitted aluminum ring that rests on top of the G10 piece as shown in figure 7.3c. We interferometrically align the microscope objective, allowing us to

glue both the G10 piece and the microscope objective in place while monitoring the system in real time to ensure that the performance remains diffraction limited even as the glue cures. Mounting the microscope ensures that the imaging system is stable with respect to the lattice. We observe very small drifts in the lattice position, less than 10% of the lattice spacing in one hour with shot to shot fluctuations of less than 15% rms.

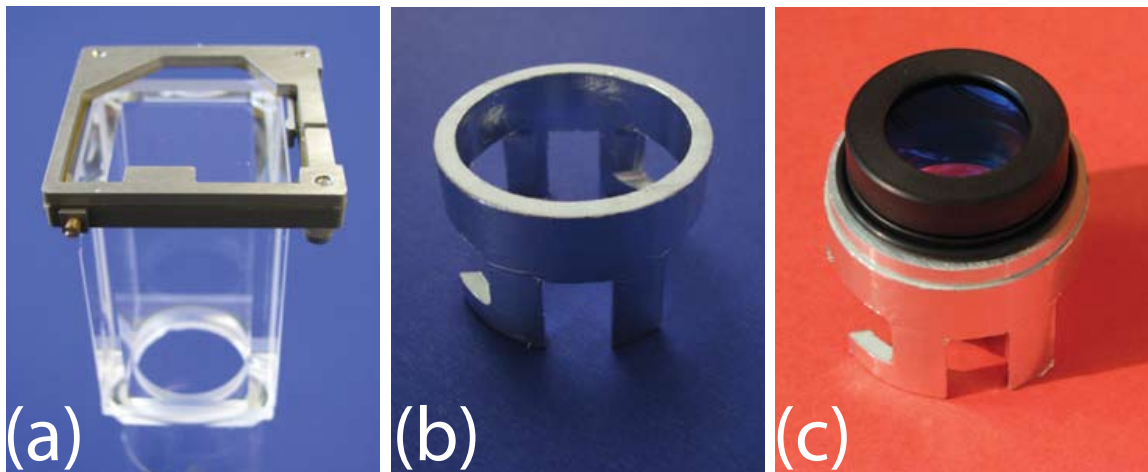


Figure 7.3: Equipment used to mount the microscope.(a) A 316 stainless steel clamp is attached to the glass cell and provides mechanical support for the microscope objective holder. A combination of insulation and appropriately placed slits allow us to avoid eddy currents.(b) A cylindrical piece of G10 is machined to hold the microscope objective. The irregular shape is a result of the constraints that the holder must rest on the stainless steel clamp in(a) as well as not restrict any of the laser beam access. The holder is tightly wrapped in aluminum foil to protect the G10 from burning by stray high power laser beams.(c) The microscope objective is then glued to a thin slitted aluminum ring that is glued to the microscope holder. This picture is for illustration only. In reality, we align the microscope *in situ* and then glue it in place.

7.4 Holographic projection of lattices

The large numerical aperture imaging system is capable of projecting lattice potentials with small lattice constants of ($a \approx 500nm$) that are compatible with the study of many-body physics. We take advantage of this capability by directly projecting a spatial light pattern [8, 36, 77] onto the atoms. Periodic phase holograms are projected onto the 2D quantum gas to create 2D lattice potentials. Potential landscapes generated in this way can be arbitrary within the limits set by the available imaging aperture and by polarization effects that can arise due to the large aperture imaging beyond the paraxial limit. Another advantage of using holographic projection is that the lattice geometry is not dependent upon the wavelength of light [78] with the exception of diffraction limits and chromatic aberrations in the lens for large wavelength changes. This allows us to use spectrally broad "white" light with a short coherence length to reduce unwanted disorder from stray interferences in a similar fashion to what was done in the EW and SW traps. Instead of using an ASE source as we did for the SW and EW traps, here we use a femtosecond laser with a spectral width of 3nm centered at 758nm to generate our far-detuned conservative lattice potentials. All experiments in this thesis were performed with a square lattice, but other geometries are easily obtainable by using a different phase pattern for the hologram. We create blue detuned square lattice potentials with a lattice constant of $a = 640nm$ and depths of up to $35E_{rec}$ where $E_{rec} = h^2/8ma^2$.

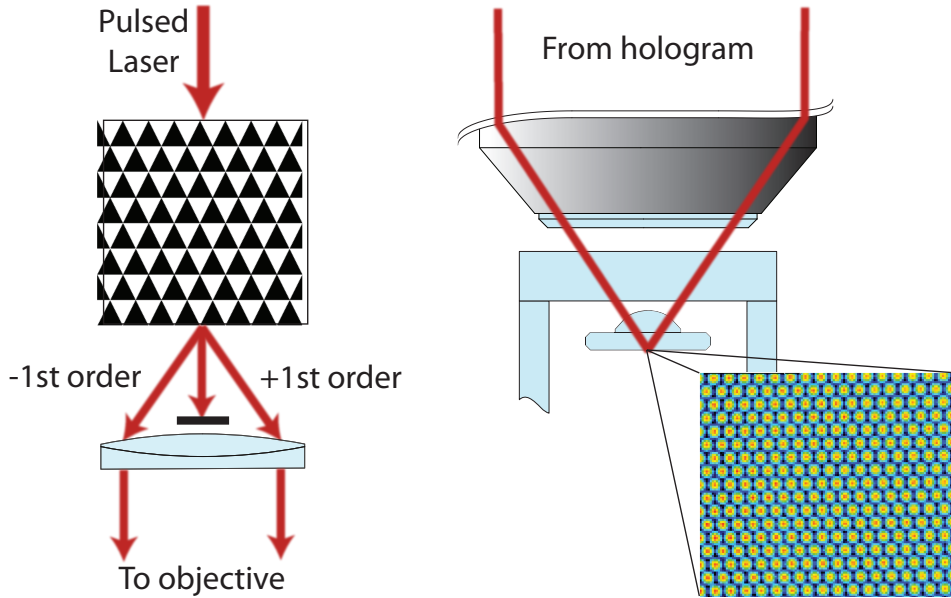


Figure 7.4: Schematic of lattice projection technique. A collimated beam is incident upon a periodic phase hologram and the resulting output is filtered and then sent to the microscope objective. After passing through the microscope objective, the beams produce an interference pattern in the same pattern as the phase hologram. Pictured is a triangular lattice that we image by capturing the reflection off of the flat face of the hemisphere.

7.4.1 2D lattice setup

The basic setup is shown in figure 7.4, a general discussion of holographic projection can be found in [13]. A collimated beam illuminates the hologram and is split into multiple diffraction orders. As we are only interested in the first diffraction orders, we block all others. The first order diffraction beams are then guided through the imaging system and onto the atoms where they create a lattice with the same shape as the hologram from which they were produced. Figure 7.4 shows actual data taken during the initial diagnostics of the holographic projection technique where a triangular phase hologram was used. In the experiment we use a square lattice and it is imperative that the polarizations of the beams be carefully controlled, other-

wise elliptically polarized light will be present in the resultant lattice. Elliptically polarized light in the lattice gives rise to effective magnetic fields [19] which are more than capable of sabotaging sub-doppler cooling mechanisms such as optical molasses. Since our detection scheme relies on a viable optical molasses we carefully control the polarization of the lattice light in order to avoid any unwanted elliptically polarized light at the local potential minima where the atoms are trapped.

A 2D square lattice requires four laser beams interfering at the position of the atoms. We design our setup such that two orthogonally polarized pairs of beams are incident upon the microscope objective. The polarizations of the beams are shown in figure 7.5 and chosen such that each pair produces a 1D lattice that is linearly polarized at the focus of the objective.

7.5 Optical molasses

With a high resolution imaging system in place and the atoms loaded into a 2D square lattice, there is nothing in principle stopping us from imaging single atoms. However, we must proceed with care. If we simply try absorption or fluorescence imaging directly, the atoms will heat up due to atomic recoil and delocalize over the lattice before we can collect enough photons to resolve their position at the single site level. It is for this reason that we employ an optical molasses [62] to cool the atoms during the imaging process. Due to the geometry of our setup the optical molasses configuration is non-standard as illustrated in figure 7.6. The molasses beams are detuned 80MHz to the red of the $F=2$ to $F'=3$ hyperfine transition. A first molasses beam is sent along the QUIC axis at a glancing incidence (15 degree) to



Figure 7.5: The four beams that create the 2D square lattice are shown entering the microscope objective. The polarization of the beams is indicated by the white arrows and chosen such that the interference pattern produced at the focus of the objective is linear at the position of the atoms.

the superpolished surface with a polarization perpendicular to the plane of incidence. This beam is then retroreflected and the polarization is rotated such that the retroreflected beam has a polarization in the plane of incidence. In this way we are able to create polarization and intensity gradients along the QUIC and vertical axes. A second molasses beam sent along the Quad axis, also at glancing incidence to the superpolished surface creates polarization gradients along the remaining axis. The molasses beam sizes are kept as small as reasonably possible (around $100\mu\text{m}$) in order to keep the power in the beams to a minimum, a few μW per beam. Excessive molasses power would result in a large amount of scatter being collected by the CCD

camera during the imaging process due to the long exposure times. We also employ the use of a repumping beam during the molasses to prevent the unwanted shelving of atoms during the detection process.

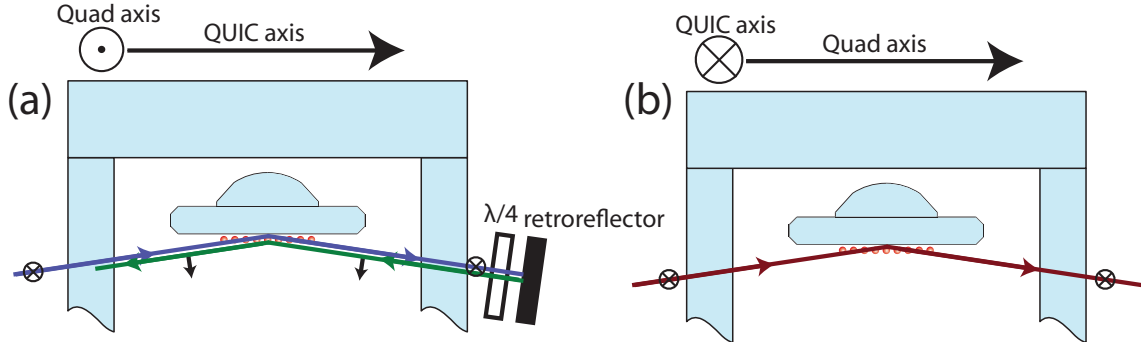


Figure 7.6: Optical molasses setup. The QUIC axis is along the Ioffe coil and Quad is along the axis of the quadrupole coils see figure 4.8.

7.6 Detection sequence

A schematic of the detection sequence is shown in figure 7.7. We begin with a 2D quantum gas in the SW trap and then adiabatically ramp up the power from the femtosecond laser source which creates a conservative 2D lattice in the plane. We then freeze the atoms in place by ramping up a very deep, near detuned pinning lattice derived from a continuous wave Ti:Sapphire laser. The pinning lattice is detuned 32GHz to the blue of the D1 line and has precisely the same geometry as the conservative 2D lattice since it is derived from the same holographic projection setup. The two axes of the pinning lattice are detuned from one another by at least 80MHz in order to time average the interference between them that would otherwise disrupt the polarization gradient cooling. For the third axis we also use near detuned light

from the Ti:Sapphire laser to increase the confinement to 3mK, this light also being frequency shifted relative to the other two axes in order to time average interferences. Once the pinning lattice is ramped up and the atom distribution is frozen in place we turn off the magnetic trap and turn on the magnetic field compensation to null the bias field at the atom position. After the magnetic fields have stabilized we then turn on the optical molasses beams. The optical molasses beams simultaneously provide sub-Doppler cooling for the atoms while scattering photons that are collected through the imaging optics. The pinning lattice depth is large compared with the equilibrium temperature of the optical molasses, allowing us to take long exposure images collecting thousands of photons per atom while holding the atoms in place.

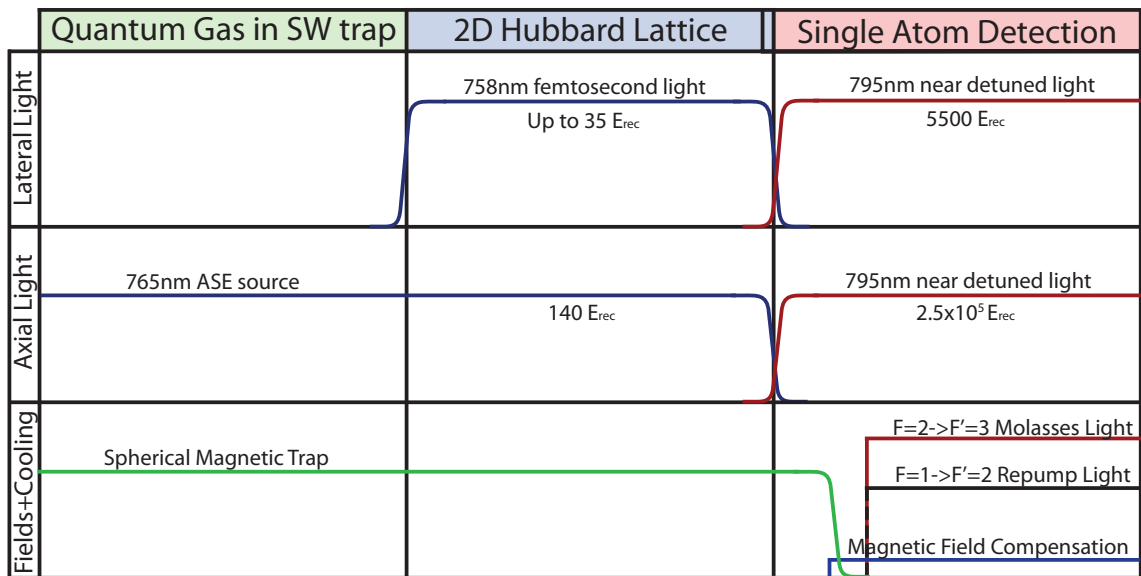


Figure 7.7: Single atom detection sequence.

7.7 Results

In initial experiments we loaded the 2D lattice with a sparse thermal cloud and then recorded an image while illuminating the atoms with an optical molasses as described previously. Analyzing such sparse clouds as shown in figure 7.8a we were able to characterize the imaging system and compare the performance with the diffraction limit as shown in figure 7.8b. We measure a single atom profile with a FWHM size of 570nm and 630nm along the x and y direction respectively, which is close to the theoretical minimum value of $\sim 520\text{nm}$. The theoretical minimum for our system is a combination of the diffraction limit of the imaging system, the initial size of the atomic wavefunction during the imaging process, and the pixel size of the camera.

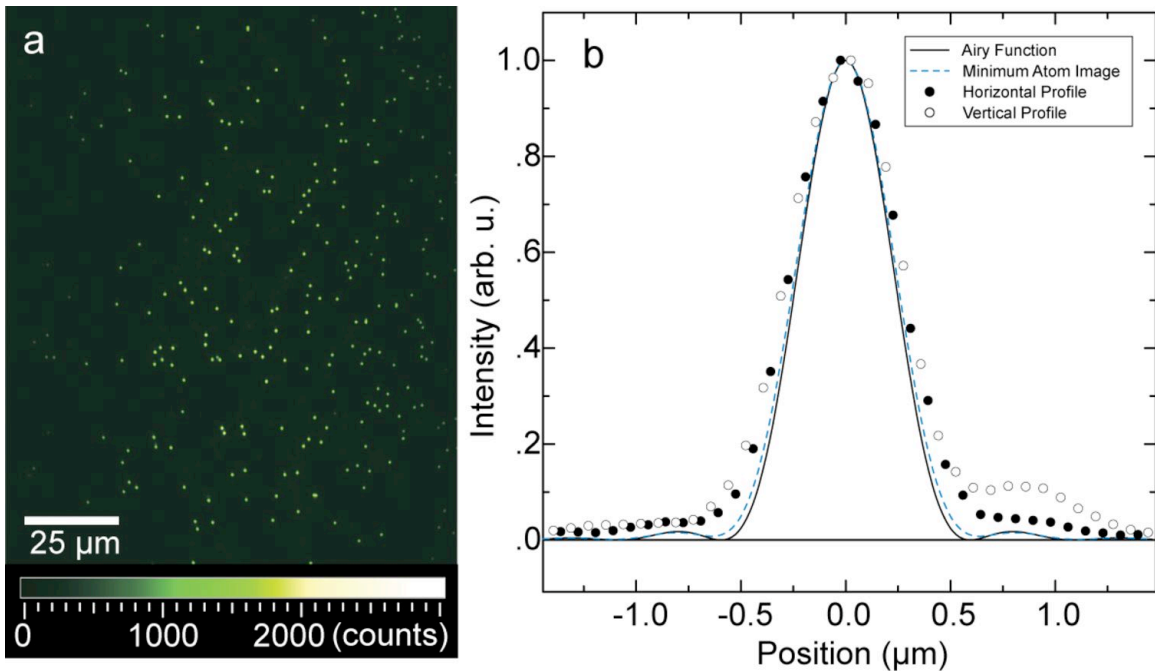


Figure 7.8: (a) CCD image of a sparse thermal cloud loaded into the 2D square lattice.(b) Response of single atom, derived from sparse image. The solid black line is the Airy function for a perfect imaging system with a numerical aperture of $\text{NA}=.8$.

Pair densities within multiply occupied lattice sites are very high due to the strong confinement in the pinning lattice. When resonantly illuminated, such pairs undergo light assisted collisions and leave the trap within a time on order of $100 \mu\text{s}$, long before they emit sufficient photons to be detected [23]. Therefore the remaining number of atoms per site is equal to the parity of the original atom number before illumination, as long as the initial occupation is small. For our molasses parameters, the collected number of photons can be up to $2 \cdot 10^4$ per atom per second, and the exposure times are typically between 200 and 1000 ms, limited by the loss of single atoms from the trap which reduces the detection fidelity. The $1/e$ lifetime in the pinning lattice is ~ 30 s, which is consistent with loss due to collisions with hot atoms in the background gas.

Figure 7.9 shows an image obtained by loading a dense condensate. The fast ramp-up of the pinning lattice within 1.5 ms switches off tunneling and projects the superfluid state wavefunction onto Poisson distributed onsite occupations with more than one atom per lattice site in the center of the trap. Due to the removal of pairs the occupation detected is lowered, typically to 42%. The images are analyzed by identifying the lattice geometry and fitting point spread functions (obtained separately by analyzing images from sparsely filled lattices) to each lattice point. As the background signal is weak and smooth due to the 2D geometry, we thus obtain the total number of scattered photons per lattice site as a simple way of determining the presence of an atom. Figure 7.10 shows the histogram of photon counts for the central region of several images with an average filling of 34%. For these pictures with long exposure times, the fidelity of identifying atoms at a given lattice site is

98%, limited by the losses occurring during the integration time. To verify that the atom distribution is preserved during imaging, we have recorded sequences of consecutive images spanning a total detection period of several seconds, during which no significant hopping occurs.

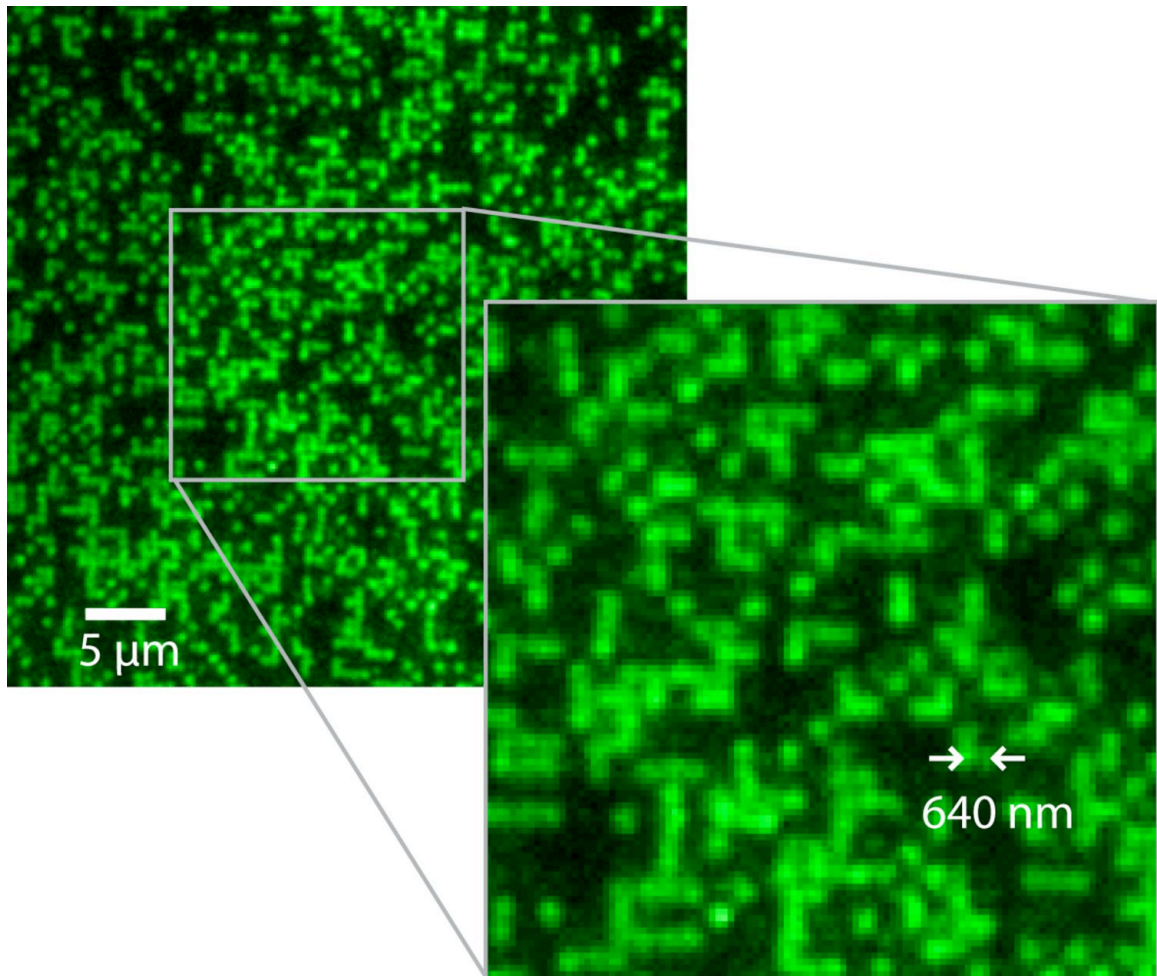


Figure 7.9: CCD image of atoms in the two dimensional square lattice.

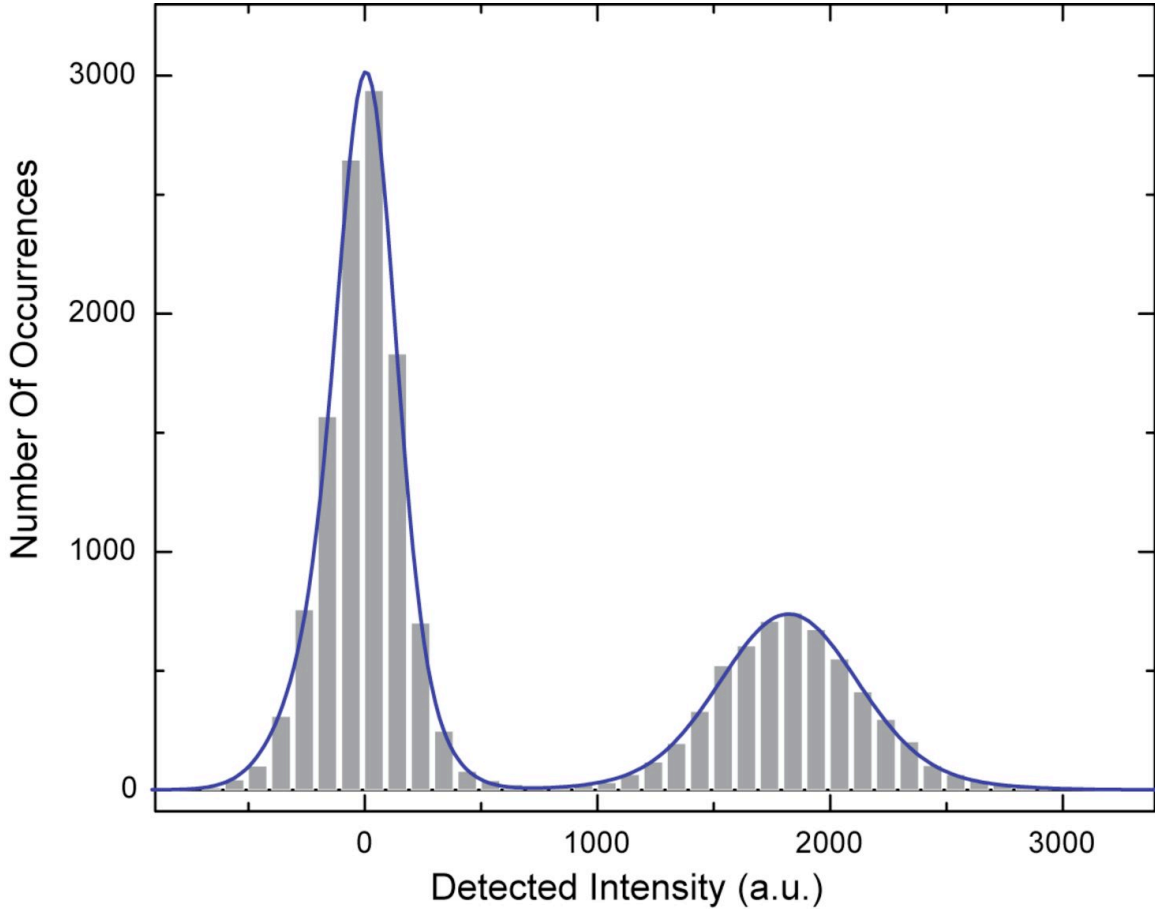


Figure 7.10: Histogram showing the distribution of the fluorescence signal collected per lattice site for an exposure time of 1s. The peak centered around zero corresponds to empty lattice sites while the second peak to the right corresponds to sites with single occupancy.

7.8 Conclusions

In the quantum gas microscope we have demonstrated a powerful new system, capable of resolving single atoms in a two dimensional optical lattice with a lattice constant small enough to explore many body physics. With the high numerical aperture of the quantum gas microscope, we have further demonstrated the use of holographic projection to create arbitrary potential landscapes, demonstrating a new

and flexible way of creating short period optical lattices.

7.9 Outlook

With the quantum gas microscope we enter a new regime in the study of optical lattices, no longer having to rely on bulk parameters alone to probe the system. With direct access to the number statistics of the lattice it will be possible in the future to directly detect strongly correlated states such as the Mott insulator and antiferromagnetic states. In our lattice configuration, the Mott transition is expected at a lattice depth of $\sim 12E_{rec}$ with a tunnel coupling strength J of 20Hz at the transition point. Lattice defects that evaded detection in past experiments will now become quantifiable and in future experiments the measurement of such defects will enable precision measurements of entropy or temperature. Local excitations such as hole-pair correlations should be accessible as well.

The method of projecting lattice potentials with lithographically patterned masks gives us full control over the lattice geometry at the single site level. In future experiments this method will allow for the creation of arbitrary potential landscapes including spin dependent landscapes which will enable the realization of large class of model Hamiltonians. The projection method also allows for the local manipulation of the quantum gas, enabling local spin flips and novel cooling schemes that will aid in the study of quantum magnetism and d -wave superfluidity.

Bibliography

- [1] C. S. Adams and E. Riis. Laser cooling and trapping of neutral atoms. *Progress in Quantum Electronics*, 21(1):1–79, 1997.
- [2] B. P. Anderson and M. A. Kasevich. Macroscopic quantum interference from atomic tunnel arrays. *Science*, 282(5394):1686–1689, 1998.
- [3] M. H. Anderson, J. R. Ensher, M. R. Matthews, C. E. Wieman, and E. A. Cornell. Observation of bose-einstein condensation in a dilute atomic vapor. *Science*, 269(5221):198–201, 1995.
- [4] M. R. Andrews, C. G. Townsend, H. J. Miesner, D. S. Durfee, D. M. Kurn, and W. Ketterle. Observation of interference between two bose condensates. *Science*, 275(5300):637–641, 1997.
- [5] N.W. Ashcroft and David N Mermin. *Solid State Physics*. Thomson Learning, Toronto, 1976.
- [6] V. I. Balykin, V. S. Letokhov, Y. B. Ovchinnikov, and A. I. Sidorov. Quantum-state selective mirror reflection of atoms by laser-light. *Physical Review Letters*, 60(21):2137–2140, 1988.
- [7] V.I. Berezinskii. Destruction of long-range order in one-dimensional and 2-dimensional systems having a continuous symmetry group 1 - classical systems. *Soviet Physics JETP-USSR*, 32(3):493, 1971.
- [8] S. Bergamini, B. Darquie, M. Jones, L. Jacubowicz, A. Browaeys, and P. Grangier. Holographic generation of microtrap arrays for single atoms by use of a programmable phase modulator. *Journal of the Optical Society of America B-Optical Physics*, 21(11):1889–1894, 2004.
- [9] J. E. Bjorkholm, R. R. Freeman, A. Ashkin, and D. B. Pearson. Observation of focusing of neutral atoms by dipole forces of resonance-radiation pressure. *Physical Review Letters*, 41(20):1361–1364, 1978.
- [10] G. C. Bjorklund. Frequency-modulation spectroscopy - new method for measuring weak absorptions and dispersions. *Optics Letters*, 5(1):15–17, 1980.

-
- [11] I. Bloch, J. Dalibard, and W. Zwerger. Many-body physics with ultracold gases. *Reviews of Modern Physics*, 80(3):885–964, 2008.
- [12] Bose. Planck’s law and light quantum hypothesis. *Zeitschrift Fur Physik*, 26:178–181, 1924.
- [13] H. Brachmann. Inducing vortices in a bose-einstein condensate using light beams with orbital angular momentum. Master’s thesis, Ludwig-Maximilians Universität Fakultät für Physik München, 2007.
- [14] Y. Castin and R. Dum. Bose-einstein condensates in time dependent traps. *Physical Review Letters*, 77(27):5315–5319, 1996.
- [15] A. Cho. Condensed-matter physics - the mad dash to make light crystals. *Science*, 320(5874):312–313, 2008. Cho, Adrian.
- [16] S. Chu, J. E. Bjorkholm, A. Ashkin, and A. Cable. Experimental-observation of optically trapped atoms. *Physical Review Letters*, 57(3):314–317, 1986.
- [17] P. Clade, C. Ryu, A. Ramanathan, K. Helmerson, and W. D. Phillips. Observation of a 2d bose gas: From thermal to quasicondensate to superfluid. *Physical Review Letters*, 102(17), 2009.
- [18] R. B. M. Clarke, T. Graf, and E. Eijs. Dipole traps with mode-locked lasers. *Applied Physics B-Lasers and Optics*, 70(5):695–700, 2000.
- [19] Claude Cohen-Tannoudji and Jacques Dupont-Roc. Experimental study of zee-man light shifts in weak magnetic fields. *Phys. Rev. A*, 5(2):968–984, Feb 1972.
- [20] S. L. Cornish, N. R. Claussen, J. L. Roberts, E. A. Cornell, and C. E. Wieman. Stable rb-85 bose-einstein condensates with widely tunable interactions. *Physical Review Letters*, 85(9):1795–1798, 2000.
- [21] F. Dalfovo, S. Giorgini, L. P. Pitaevskii, and S. Stringari. Theory of bose-einstein condensation in trapped gases. *Reviews of Modern Physics*, 71(3):463–512, 1999.
- [22] K. B. Davis, M. O. Mewes, M. R. Andrews, N. J. Vandruten, D. S. Durfee, D. M. Kurn, and W. Ketterle. Bose-einstein condensation in a gas of sodium atoms. *Physical Review Letters*, 75(22):3969–3973, 1995.
- [23] M. T. DePue, C. McCormick, S. L. Winoto, S. Oliver, and D. S. Weiss. Unity occupation of sites in a 3d optical lattice. *Physical Review Letters*, 82(11):2262–2265, 1999.

- [24] S. Dettmer, D. Hellweg, P. Ryytty, J. J. Arlt, W. Ertmer, K. Sengstock, D. S. Petrov, G. V. Shlyapnikov, H. Kreutzmann, L. Santos, and M. Lewenstein. Observation of phase fluctuations in elongated bose-einstein condensates. *Physical Review Letters*, 8716(16):art. no.–160406, 2001.
- [25] A. Einstein. Quantum theory of monatomic ideal gases. *Sitzungsberichte Der Preussischen Akademie Der Wissenschaften Physikalisch-Mathematische Klasse*, pages 261–267, 1924.
- [26] B. Engeser. *A novel surface trapping apparatus for ultracold cesium atoms and the investigation of an Efimov resonance*. PhD thesis, Universität Innsbruck, 2006.
- [27] T. Esslinger, I. Bloch, and T. W. Hansch. Bose-einstein condensation in a quadrupole-ioffe-configuration trap. *Physical Review A*, 58(4):R2664–R2667, 1998.
- [28] M. P. A. Fisher, P. B. Weichman, G. Grinstein, and D. S. Fisher. Boson localization and the superfluid-insulator transition. *Physical Review B*, 40(1):546–570, 1989.
- [29] N. Gemelke, X. B. Zhang, C. L. Hung, and C. Chin. In situ observation of incompressible mott-insulating domains in ultracold atomic gases. *Nature*, 460(7258):995–U75, 2009.
- [30] T. Gericke, P. Wurtz, D. Reitz, T. Langen, and H. Ott. High-resolution scanning electron microscopy of an ultracold quantum gas. *Nature Physics*, 4(12):949–953, 2008. Gericke, Tatjana Wuertz, Peter Reitz, Daniel Langen, Tim Ott, Herwig.
- [31] J.I. Gillen, W.S. Bakr, A Peng, S Fölling, and M Greiner. Hybrid 2d surface trap for quantum simulation. *ArXiv:0812.3630*, 2008.
- [32] A. Gorlitz, J. M. Vogels, A. E. Leanhardt, C. Raman, T. L. Gustavson, J. R. Abo-Shaeer, A. P. Chikkatur, S. Gupta, S. Inouye, T. Rosenband, and W. Ketterle. Realization of bose-einstein condensates in lower dimensions. *Physical Review Letters*, 8713(13), 2001.
- [33] M. Greiner. *Ultracold quantum gases in three-dimensional optical lattice potentials*. PhD thesis, Ludwig-Maximilians-Universität München, 2003.
- [34] M. Greiner, I. Bloch, T. W. Hänsch, and T. Esslinger. Magnetic transport of trapped cold atoms over a large distance. *Phys. Rev. A*, 63(3), 2001.
- [35] M. Greiner, O. Mandel, T. Esslinger, T. W. Hänsch, and I. Bloch. Quantum phase transition from a superfluid to a mott insulator in a gas of ultracold atoms. *Nature*, 415(6867):39–44, 2002.

-
- [36] D. G. Grier. A revolution in optical manipulation. *Nature*, 424(6950):810–816, 2003.
- [37] D.J. Griffiths. *Introduction to Quantum Mechanics*. Prentice Hall, Upper Saddle River, New Jersey 07458, 1995.
- [38] R. Grimm, M. Weidemuller, and Y. B. Ovchinnikov. Optical dipole traps for neutral atoms. *Advances in Atomic Molecular, and Optical Physics, Vol. 42*, 42:95–170, 2000.
- [39] R. Grimm, M. Weidemuller, and Y. B. Ovchinnikov. Optical dipole traps for neutral atoms. *Advances in Atomic Molecular, and Optical Physics, Vol. 42*, 42:95–170, 2000.
- [40] E. P. Gross. Structure of a quantized vortex in boson systems. *Nuovo Cimento*, 20(3):454, 1961.
- [41] M. Hammes, D. Rychtarik, B. Engeser, H. C. Nagerl, and R. Grimm. Evanescent-wave trapping and evaporative cooling of an atomic gas at the crossover to two dimensions. *Physical Review Letters*, 90(17), 2003.
- [42] Eugene Hecht. *Optics, Third Edition*. Addison Wesley Longman, New York, 1998.
- [43] J. Hubbard. Electron correlations in narrow energy bands. *Proceedings of the Royal Society of London Series a-Mathematical and Physical Sciences*, 276(DEC):238, 1963.
- [44] J.D. Jackson. *Classical Electrodynamics*. John Wiley and Sons, Inc., Hoboken, NJ, 1976.
- [45] D. Jaksch, C. Bruder, J. I. Cirac, C. W. Gardiner, and P. Zoller. Cold bosonic atoms in optical lattices. *Physical Review Letters*, 81(15):3108–3111, 1998.
- [46] P. S. Jessen and I. H. Deutsch. Optical lattices. In *Advances in Atomic, Molecular, and Optical Physics, Vol 37*, volume 37 of *Advances in Atomic Molecular and Optical Physics*, pages 95–138. 1996.
- [47] R. Jordens, N. Strohmaier, K. Gunther, H. Moritz, and T. Esslinger. A mott insulator of fermionic atoms in an optical lattice. *Nature*, 455(7210):204–U34, 2008. Joerdens, Robert Strohmaier, Niels Guenther, Kenneth Moritz, Henning Esslinger, Tilman.
- [48] Y. Kagan, E. L. Surkov, and G. V. Shlyapnikov. Evolution of a bose-condensed gas under variations of the confining potential. *Physical Review A*, 54(3):R1753–R1756, 1996.

- [49] W. Ketterle, D. Durfee, and D. Stamper-Kurn. Making, probing and understanding bose-einstein condensates. In M. Inguscio, S. Stringari, and C.E. Wieman, editors, *Proceedings of the International School of Physics - Enrico Fermi*. IOS Press, 1999.
- [50] W. Ketterle and N. J. VanDruten. Evaporative cooling of trapped atoms. In *Advances in Atomic, Molecular, and Optical Physics, Vol 37*, volume 37 of *Advances in Atomic Molecular and Optical Physics*, pages 181–236. 1996.
- [51] C. Kittel. *Quantum Theory of Solids*. John Wiley and Sons, New York, 1963.
- [52] M. Kohl, H. Moritz, T. Stoferle, K. Gunter, and T. Esslinger. Fermionic atoms in a three dimensional optical lattice: Observing fermi surfaces, dynamics, and interactions. *Physical Review Letters*, 94(8), 2005.
- [53] J. M. Kosterlitz and D. J. Thouless. Ordering, metastability and phase-transitions in 2 dimensional systems. *Journal of Physics C-Solid State Physics*, 6(7):1181–1203, 1973.
- [54] R. D. Kronig and W. G. Penney. Quantum mechanics of electrons on crystal lattices. *Proceedings of the Royal Society of London Series a-Containing Papers of a Mathematical and Physical Character*, 130(814):499–513, 1931.
- [55] A. Landragin, G. Labeyrie, C. Henkel, R. Kaiser, N. Vansteenkiste, C. I. Westbrook, and A. Aspect. Specular versus diffuse reflection of atoms from an evanescent-wave mirror. *Optics Letters*, 21(19):1591–1593, 1996.
- [56] E. Majorana. Atomi orientate in campo magnetico variabile. *Nuovo Cimento*, 9(43):2631–2634, 1933.
- [57] S. M. Mansfield and G. S. Kino. Solid immersion microscope. *Applied Physics Letters*, 57(24):2615–2616, 1990.
- [58] J. M. McGuirk, D. M. Harber, J. M. Obrecht, and E. A. Cornell. Alkali-metal adsorbate polarization on conducting and insulating surfaces probed with bose-einstein condensates. *Physical Review A*, 69(6), 2004.
- [59] H. Metcalf and P. van der Straten. *Laser Cooling and Trapping*. Springer, New York, 1999.
- [60] O. Morsch and M. Oberthaler. Dynamics of bose-einstein condensates in optical lattices. *Reviews of Modern Physics*, 78(1):179–215, 2006.
- [61] D. R. Nelson and J. M. Kosterlitz. Universal jump in superfluid density of 2-dimensional superfluids. *Physical Review Letters*, 39(19):1201–1205, 1977.

- [62] K. D. Nelson, X. Li, and D. S. Weiss. Imaging single atoms in a three-dimensional array. *Nature Physics*, 3(8):556–560, 2007.
- [63] J. M. Obrecht, R. J. Wild, and E. A. Cornell. Measuring electric fields from surface contaminants with neutral atoms. *Physical Review A*, 75(6), 2007. Obrecht, J. M. Wild, R. J. Cornell, E. A.
- [64] H. Ott, E. de Mirandes, F. Ferlaino, G. Roati, V. Turck, G. Modugno, and M. Inguscio. Radio frequency selective addressing of localized atoms in a periodic potential. *Physical Review Letters*, 93(12), 2004.
- [65] Y. B. Ovchinnikov, I. Manek, and R. Grimm. Surface trap for cs atoms based on evanescent-wave cooling. *Physical Review Letters*, 79(12):2225–2228, 1997.
- [66] C. Pethick and H. Smith. *Bose Einstein Condensation in Dilute Gases*. Cambridge University Press, Cambridge, 2001.
- [67] D. S. Petrov, D. M. Gangardt, and G. V. Shlyapnikov. Low-dimensional trapped gases. volume 116, pages 5–44, 2004.
- [68] D. S. Petrov, M. Holzmann, and G. V. Shlyapnikov. Bose-einstein condensation in quasi-2d trapped gases. *Physical Review Letters*, 84(12):2551–2555, 2000.
- [69] W. D. Phillips. Laser cooling and trapping of neutral atoms. *Reviews of Modern Physics*, 70(3):721–741, 1998.
- [70] L. P. Pitaevskii. Vortex lines in an imperfect bose gas. *Soviet Physics JETP-USSR*, 13(2):451–454, 1961.
- [71] N. Prokof'ev, O. Ruebenacker, and B. Svistunov. Critical point of a weakly interacting two-dimensional bose gas. *Physical Review Letters*, 87(27), 2001.
- [72] E. L. Raab, M. Prentiss, A. Cable, S. Chu, and D. E. Pritchard. Trapping of neutral sodium atoms with radiation pressure. *Physical Review Letters*, 59(23):2631–2634, 1987.
- [73] Lord Rayleigh. A study of glass surfaces in optical contact. *Proceedings of the Royal Society of London. Series A, Mathematical and Physical Sciences*, 156(888):326–349, 1936.
- [74] L. Ricci, M. Weidemuller, T. Esslinger, A. Hemmerich, C. Zimmermann, V. Vuletic, W. Konig, and T. W. Hansch. A compact grating-stabilized diode-laser system for atomic physics. *Optics Communications*, 117(5-6):541–549, 1995.
- [75] D. Rychtarik, B. Engeser, H. C. Nagerl, and R. Grimm. Two-dimensional bose-einstein condensate in an optical surface trap. *Physical Review Letters*, 92(17), 2004.

-
- [76] R. Scheunemann, F. S. Cataliotti, T. W. Hansch, and M. Weitz. Resolving and addressing atoms in individual sites of a co2-laser optical lattice. *Physical Review A*, 62(5):art. no.–051801, 2000.
- [77] J. Sebby-Strabley, R. T. R. Newell, J. O. Day, E. Brekke, and T. G. Walker. High-density mesoscopic atom clouds in a holographic atom trap. *Physical Review A*, 71(2), 2005.
- [78] K. A. B. Soderberg, N. Gemelke, and C. Chin. Ultracold molecules: vehicles to scalable quantum information processing. *New Journal of Physics*, 11, 2009.
- [79] I. B. Spielman, W. D. Phillips, and J. V. Porto. Mott-insulator transition in a two-dimensional atomic bose gas. *Physical Review Letters*, 98(8), 2007. Spielman, I. B. Phillips, W. D. Porto, J. V.
- [80] S. Stock, Z. Hadzibabic, B. Battelier, M. Cheneau, and J. Dalibard. Observation of phase defects in quasi-two-dimensional bose-einstein condensates. *Physical Review Letters*, 95(19), 2005.
- [81] E. Tiesinga, A. J. Moerdijk, B. J. Verhaar, and H. T. C. Stoof. Conditions for bose-einstein condensation in magnetically trapped atomic cesium. *Physical Review A*, 46(3):R1167–R1170, 1992.
- [82] E. Tiesinga, B. J. Verhaar, and H. T. C. Stoof. Threshold and resonance phenomena in ultracold ground-state collisions. *Physical Review A*, 47(5):4114–4122, 1993. Part B.
- [83] V. Vuletic, C. Chin, A. J. Kerman, and S. Chu. Degenerate raman sideband cooling of trapped cesium atoms at very high atomic densities. *Physical Review Letters*, 81(26):5768–5771, 1998.
- [84] G. H. Wannier. The structure of electronic excitation levels in insulating crystals. *Physical Review*, 52(3):0191–0197, 1937.

Appendix A

Rubidium data

The data in the following pages is taken from Dan Steck's fantastic alkali data sheet for Rubidium. Please visit <http://steck.us/alkalidata/> for a complete reference on the properties of ^{87}Rb .

Table 1: Fundamental Physical Constants (2006 CODATA recommended values [2])

Speed of Light	c	$2.997\,924\,58 \times 10^8$ m/s (exact)
Permeability of Vacuum	μ_0	$4\pi \times 10^{-7}$ N/A ² (exact)
Permittivity of Vacuum	ϵ_0	$(\mu_0 c^2)^{-1}$ (exact) $= 8.854\,187\,817 \dots \times 10^{-12}$ F/m
Planck's Constant	h	$6.626\,068\,96(33) \times 10^{-34}$ J·s $4.135\,667\,33(10) \times 10^{-15}$ eV·s
	\hbar	$1.054\,571\,628(53) \times 10^{-34}$ J·s $6.582\,118\,99(16) \times 10^{-16}$ eV·s
Elementary Charge	e	$1.602\,176\,487(40) \times 10^{-19}$ C
Bohr Magneton	μ_B	$9.274\,009\,15(23) \times 10^{-24}$ J/T
		$h \cdot 1.399\,624\,604(35)$ MHz/G
Atomic Mass Unit	u	$1.660\,538\,782(83) \times 10^{-27}$ kg
Electron Mass	m_e	$5.485\,799\,0943(23) \times 10^{-4}$ u
		$9.109\,382\,15(45) \times 10^{-31}$ kg
Bohr Radius	a_0	$0.529\,177\,208\,59(36) \times 10^{-10}$ m
Boltzmann's Constant	k_B	$1.380\,6504(24) \times 10^{-23}$ J/K

Table 2: Rubidium 87 Physical Properties.

Atomic Number	Z	37	
Total Nucleons	$Z + N$	87	
Relative Natural Abundance	$\eta(^{87}\text{Rb})$	27.83(2)%	[3]
Nuclear Lifetime	τ_n	4.88×10^{10} yr	[3]
Atomic Mass	m	86.909 180 520(15) u	[4]
		$1.443\,160\,648(72) \times 10^{-25}$ kg	
Density at 25°C	ρ_m	1.53 g/cm ³	[3]
Melting Point	T_M	39.30 °C	[3]
Boiling Point	T_B	688 °C	[3]
Specific Heat Capacity	c_p	0.363 J/g·K	[3]
Molar Heat Capacity	C_p	31.060 J/mol·K	[3]
Vapor Pressure at 25°C	P_v	$3.92(20) \times 10^{-7}$ torr	[5]
Nuclear Spin	I	3/2	
Ionization Limit	E_I	33 690.804 80(20) cm ⁻¹	[8]
		4.177 127 06(10) eV	

Table 3: Rubidium 87 D₂ ($5^2S_{1/2} \rightarrow 5^2P_{3/2}$) Transition Optical Properties.

Frequency	ω_0	$2\pi \cdot 384.230\,484\,468\,5(62)$ THz	[9]
Transition Energy	$\hbar\omega_0$	1.589 049 462(38) eV	
Wavelength (Vacuum)	λ	780.241 209 686(13) nm	
Wavelength (Air)	λ_{air}	780.033 330(23) nm	
Wave Number (Vacuum)	$k_L/2\pi$	12 816.549 389 93(21) cm ⁻¹	
Isotope shift	$\omega_0(^{87}\text{Rb}) - \omega_0(^{85}\text{Rb})$	$2\pi \cdot 78.095(12)$ MHz	[10]
Lifetime	τ	26.2348(77) ns	[18–21]
Decay Rate/ Natural Line Width (FWHM)	Γ	$38.117(11) \times 10^6$ s ⁻¹ $2\pi \cdot 6.0666(18)$ MHz	
Absorption oscillator strength	f	0.695 77(29)	
Recoil Velocity	v_r	5.8845 mm/s	
Recoil Energy	ω_r	$2\pi \cdot 3.7710$ kHz	
Recoil Temperature	T_r	361.96 nK	
Doppler Shift ($v_{\text{atom}} = v_r$)	$\Delta\omega_d(v_{\text{atom}} = v_r)$	$2\pi \cdot 7.5419$ kHz	
Doppler Temperature	T_D	145.57 μ K	
Frequency shift for standing wave moving with $v_{\text{sw}} = v_r$	$\Delta\omega_{\text{sw}}(v_{\text{sw}} = v_r)$	$2\pi \cdot 15.0839$ kHz	

Table 4: Rubidium 87 D₁ ($5^2S_{1/2} \rightarrow 5^2P_{1/2}$) Transition Optical Properties.

Frequency	ω_0	$2\pi \cdot 377.107\,463\,380(11)$ THz	[10]
Transition Energy	$\hbar\omega_0$	1.559 591 016(38) eV	
Wavelength (Vacuum)	λ	794.978 851 156(23) nm	
Wavelength (Air)	λ_{air}	794.767 119(24) nm	
Wave Number (Vacuum)	$k_L/2\pi$	12 578.950 981 47(37) cm ⁻¹	
Isotope shift	$\omega_0(^{87}\text{Rb}) - \omega_0(^{85}\text{Rb})$	$2\pi \cdot 77.583(12)$ MHz	[10]
Lifetime	τ	27.679(27) ns	[18, 19, 21]
Decay Rate/ Natural Line Width (FWHM)	Γ	$36.129(35) \times 10^6$ s ⁻¹ $2\pi \cdot 5.7500(56)$ MHz	
Absorption oscillator strength	f	0.342 31(97)	
Recoil Velocity	v_r	5.7754 mm/s	
Recoil Energy	ω_r	$2\pi \cdot 3.6325$ kHz	
Recoil Temperature	T_r	348.66 nK	
Doppler Shift ($v_{\text{atom}} = v_r$)	$\Delta\omega_d(v_{\text{atom}} = v_r)$	$2\pi \cdot 7.2649$ kHz	
Frequency shift for standing wave moving with $v_{\text{sw}} = v_r$	$\Delta\omega_{\text{sw}}(v_{\text{sw}} = v_r)$	$2\pi \cdot 14.5298$ kHz	

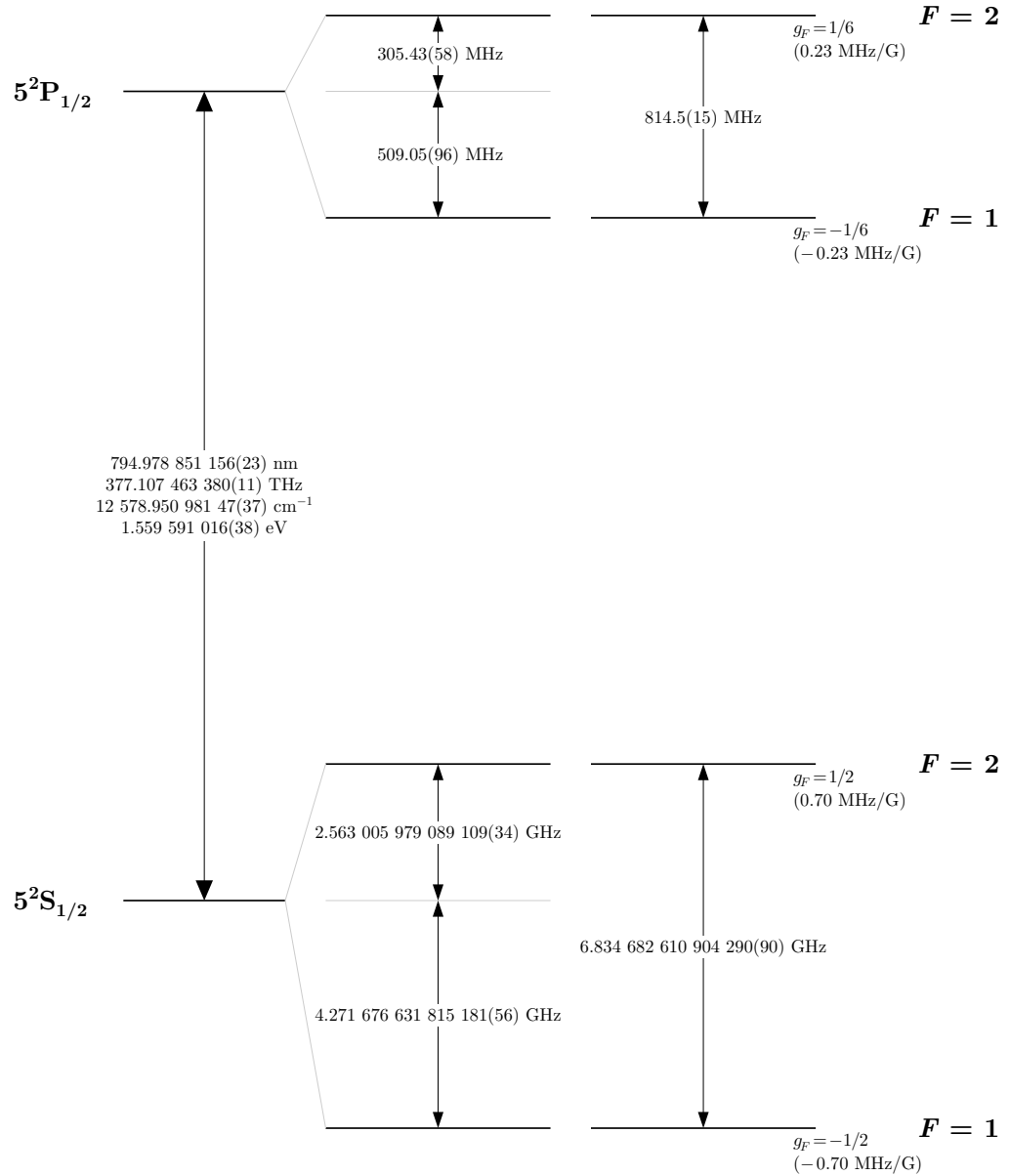


Figure 3: Rubidium 87 D_1 transition hyperfine structure, with frequency splittings between the hyperfine energy levels. The excited-state values are taken from [10, 11, 26], and the ground-state values are from [29]. The relative hyperfine shifts are shown to scale within each hyperfine manifold (but visual spacings should not be compared between manifolds or to the optical splitting). The approximate Landé g_F -factors for each level are also given, with the corresponding Zeeman splittings between adjacent magnetic sublevels.

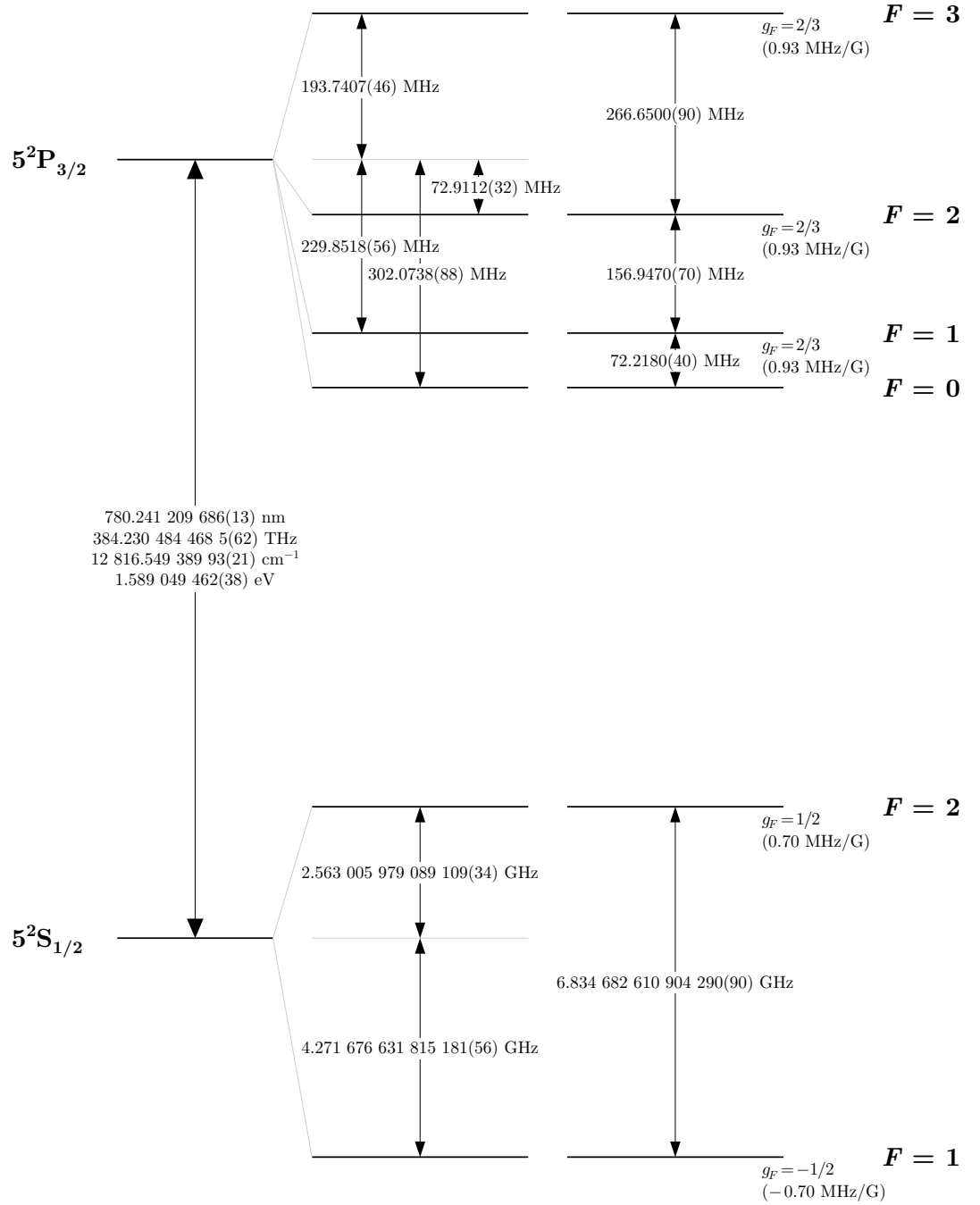
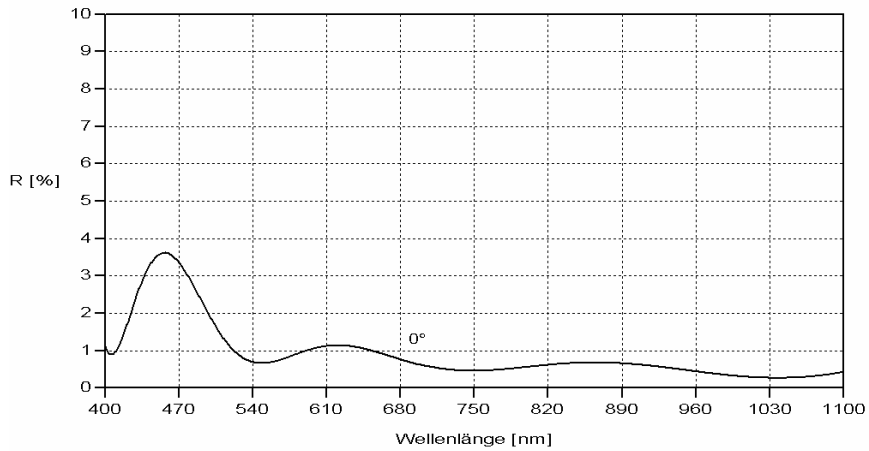
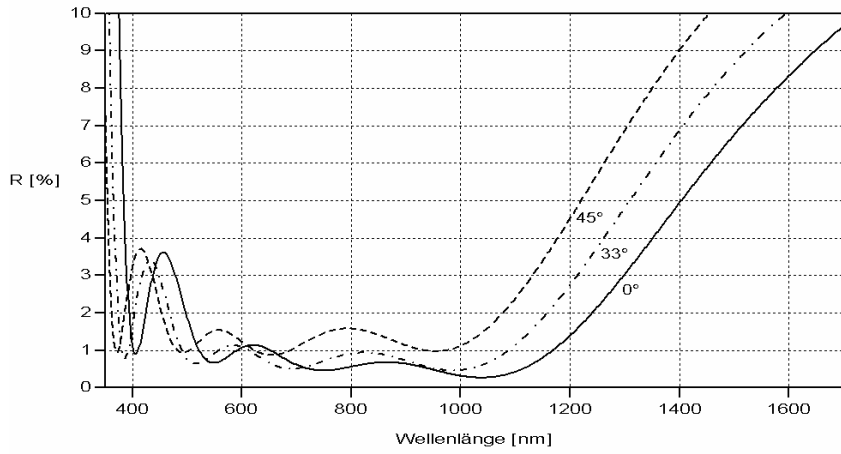


Figure 2: Rubidium 87 D_2 transition hyperfine structure, with frequency splittings between the hyperfine energy levels. The excited-state values are taken from [9], and the ground-state values are from [29]. The relative hyperfine shifts are shown to scale within each hyperfine manifold (but visual spacings should not be compared between manifolds or to the optical splitting). The approximate Landé g_F -factors for each level are also given, with the corresponding Zeeman splittings between adjacent magnetic sublevels.

Appendix B

Anti-reflection coating curves

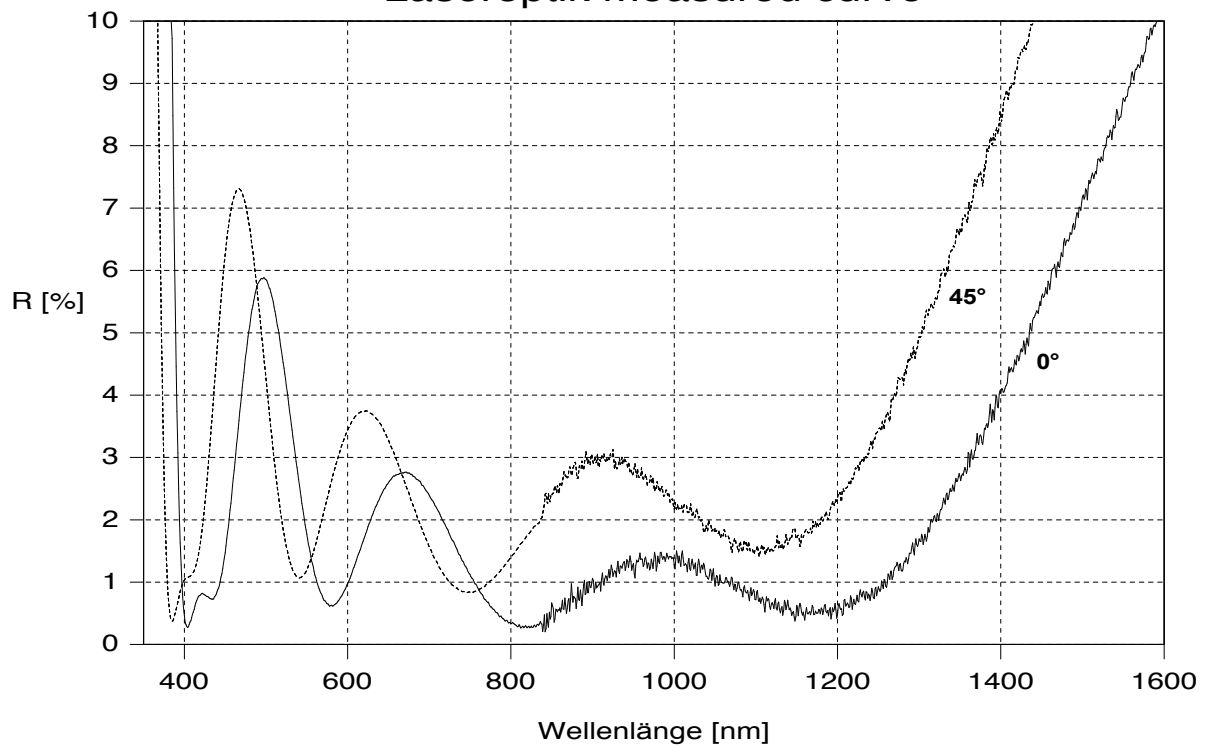
Specified and measured coatings on the glass cell.



B-02224: AR400-420+532-670+766-1064HT-1600nm/0-45°

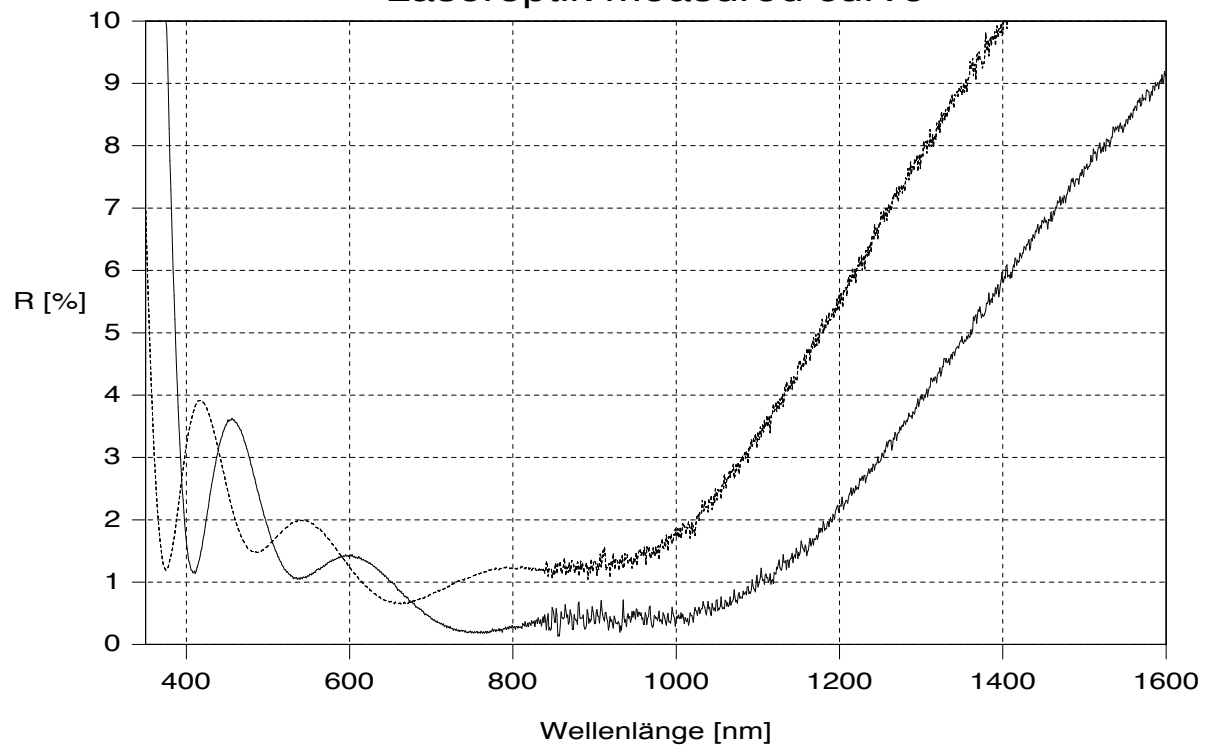
λ [nm]	R(0°) < [%]	R(33°) < [%]	R(45°) < [%]
400-420	4	5	8
532-670	1,8	2	3
766-1064	1	1,5	2,5
400-750	5	-	-
750-1064	1,5	-	-
760-910	1	-	-
1064-1600	10	-	-

01037C2: Beschichtung B-02336-02 auf Boden
Laseroptik measured curve



01037C2b.SP
01037C2a.SP

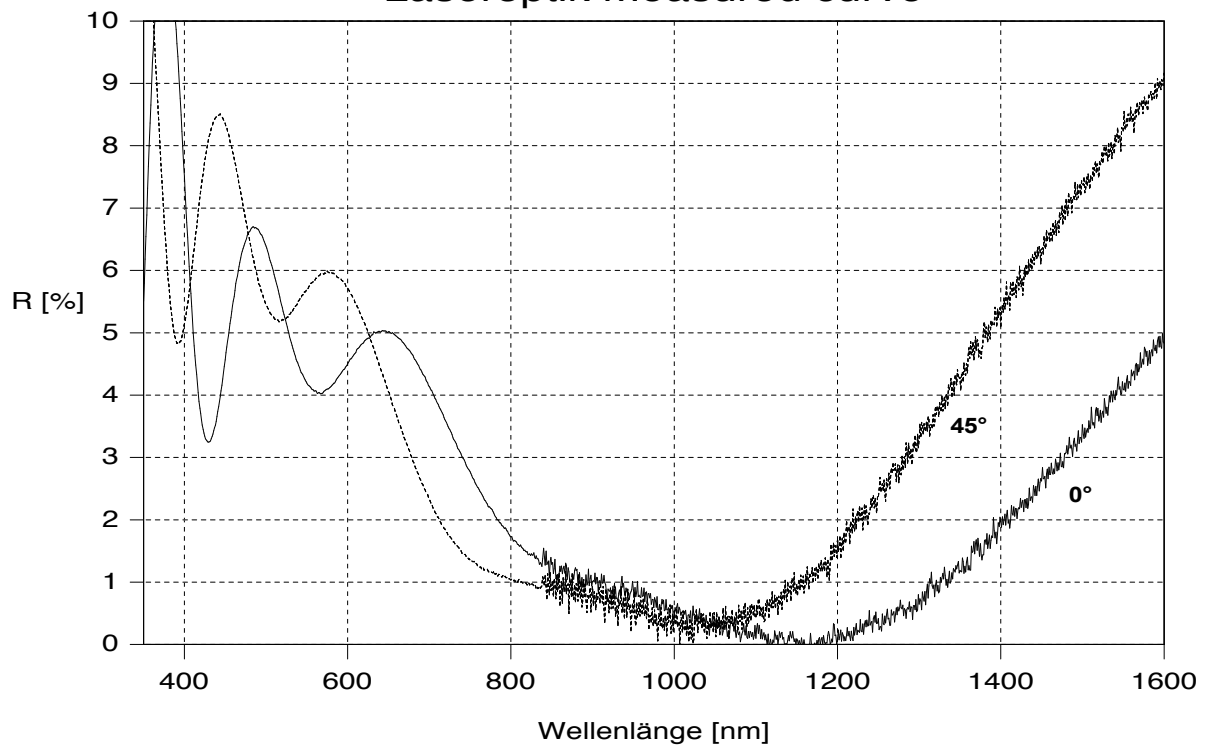
15037H2: Beschichtung B-02336 auf Mantelflächen
Laseroptik measured curve



15037h2b.SP
15037h2a.SP

15037H2: Beschichtung B-02336 auf Mantelfläche #1

Laseroptik measured curve



15037h2d.SP
15037h2c.SP

